Crystallization Process Development and Spherical Agglomerates for Pharmaceutical Processing Applications

by

Justin Quon

B.S. Chemical Engineering

University of Delaware, 2007

M. S. Chemical Engineering Practice

Massachusetts Institute of Technology, 2009

Submitted to the Department of Chemical Engineering in partial fulfillment of the requirements for the degree of

Doctor of Philosophy

at the

MASSACHUSETTS INSTITUTE OF TECHNOLOGY

February 2013

Signature of Author: _____
Department of Chemical Engineering
October 18, 2012

Certified by: _____
Bernhardt Trout
Professor of Chemical Engineering
Thesis Supervisor

Certified by: _____
T. Alan Hatton
Professor of Chemical Engineering
Thesis Supervisor

Accepted by: _____
Patrick Doyle
Professor of Chemical Engineering
Chairman, Committee for Graduate Students

Crystallization Process Development and Spherical Agglomerates for Pharmaceutical Processing Applications

By

Justin Louie Quon

Submitted to the Chemical Engineering Department on October 18, 2012, in partial fulfillment of the requirements for the degree of
Doctor of Philosophy

ABSTRACT

The control of crystallization steps is essential in the production of many materials in the pharmaceutical, materials, and chemical industries. Additionally, due to increasing costs of research and development, reductions in manufacturing costs by moving from batch to continuous manufacturing are necessary to sustain profitability of the pharmaceutical industry. Two different projects were researched to progress towards this goal. The first was the demonstration of a continuous manufacturing platform. The second goal was the development of new crystallization techniques.

Two continuous crystallization processes were developed as part of a demonstration unit for continuous manufacturing of Aliskiren hemifumarate. The first process was an anti-solvent crystallization of an intermediate. The second process was a continuous reactive crystallization developed for the final product. The processes were able to crystallize the two compounds with both high yield (>90%) and purity (>99%). Population balance modeling was performed and experimental data were fit to the model to obtain kinetic parameters for crystal growth and nucleation for both systems. The models were used to optimize crystal purity and yield of the products.

In addition, this thesis describes two separate projects involving spherical agglomerates. In the first study, acetaminophen was shown to crystallize significantly faster in the presence of spherical agglomerates of lactose than single crystal lactose. An epitaxy study and molecular dynamics simulations showed that the $(14\bar{1})/(001)$ pairing of faces showed coincident lattice matching and favorable energy interaction. Maximizing the number of substrate faces available for interaction increases the chance for a lattice match between the substrate and the crystallizing material which can be useful for controlling and increasing nucleation kinetics.

Finally, water-in-oil emulsions were used to make composite spherical agglomerates with two components: a heterosurface, and a target compound that does not typically crystallize as spherical agglomerates on its own. The generated composite agglomerates were relatively monodisperse and were characterized using optical microscopy, scanning electron microscopy, x-ray powder diffraction, and differential scanning calorimetry. This technique could potentially be applied to other hydrophilic compounds, in particular water-soluble pharmaceuticals

compounds, in order to change crystal morphology to spherical agglomerates in order to simplify downstream processing.

Thesis Supervisors:

Bernhardt Trout
Title: Professor of Chemical Engineering

T. Alan Hatton
Title: Ralph Landau Professor of Chemical Engineering

ACKNOWLEDGEMENTS

I've had a great time at MIT over the last 5+ years at the Chemical Engineering Department and I wouldn't have made it without help and support from a number of people.

First and foremost I want to thank my thesis advisors Prof. Bernhardt Trout and Prof. Alan Hatton. Without their guidance and advice I would have struggled much more with research and to finish my Ph.D. than I did. I also want to thank my thesis committee members, Prof. Allan Myerson and Prof. Klavs Jensen for all of their help throughout the past few years.

I would like to thank my main collaborators throughout my Ph.D.: Dr. Keith Chadwick, Dr. Haitao Zhang, and Dr. Geoffrey Wood. Keith taught me so much about nucleation theory and solid state characterization, and really helped me with the heterogeneous nucleation projects. Without Haitao's contributions we probably never would have finished the red-line project. And without Geoff, we never would have finished the molecular dynamics simulations for the spherical agglomerates projects.

I also want to thank the Hatton, Trout, and Myerson groups, and the Redline team for all of their discussions and comments throughout the years. In particular, I want to thank Jie, Eve, Blair, Kitae, Andy, Nate, Mike, Patrick, and Jose for their friendship and camaraderie.

I wouldn't have survived the past few years without the support of both friends and family. I want to thank Byron, Stephen, Josh, Adel, Kay, Jaisree, Bradley, and Irene for always being there when I needed a friend. Finally, I want to thank my parents Check and Wailan, my siblings Nicole, Toshio, Daniel, and Denise, and my girlfriend Amanda for their love and patience.

Table of Contents

List of Figures

List of Tables

1. INTRODUCTION

1.1. Need for Continuous Manufacturing

The cost of manufacturing pharmaceuticals has becoming increasingly expensive over the recent years. A study performed in 2003 by Dimasi showed the ever increasing cost of research and development of new drugs, and showed that it increased significantly faster than the rate of inflation, and faster than the rate of new drug discovery [1]. In addition, the increased prevalence of generics companies has increased competition and reduced sales volumes for drug innovators [2, 3]. Because of rising costs of discovery and research, once a drug has actually been developed, reducing the production costs as much as possible is paramount to retaining profitability. Manufacturing costs can account for up to 30% of the total cost of producing a pharmaceutical product [3]. If this amount can be reduced significantly, the profitability of producing drugs can be increased. Continuous manufacturing is seen as one of the leading ways to decrease production costs while maintaining or even improving drug quality. Significant research has already been done to develop new technologies that could be used to continuously produce pharmaceutical products. This includes work studying new methods to perform reactions [4-6], crystallizations [7, 8], and downstream processing [9-12]. Crystallizations in particular are an area where significant progress can be made to improve downstream processing.

1.2. Crystallization Background

Crystallization is an important separation and purification process for a number of products in a multitude of industries. Many manufacturing processes in industries such as chemicals, foods, and pharmaceuticals include a crystallization step as either an intermediate purification or final isolation step [13]. Crystallization processes are designed to obtain crystals with controlled purity, size, shape, and polymorphic form in high yield. For final crystallization

steps of pharmaceutical products, the control of crystal size, shape, and form is crucial as these properties can influence downstream operations such as filtration, drying, and milling as well as influence the physical and chemical properties such as dissolution rate and solubility [14, 15]. Additionally, purity and yield of the product are very important parameters, the prior to ensure that the product meets specification, the latter to maximize production. Knowledge of the process conditions required to fabricate crystals with controlled characteristics is critical during process development.

Pharmaceutical crystallizations are typically performed in batch, using cooling, addition of anti-solvent, and reaction to generate supersaturation. Although the methodologies for developing these types of batch crystallization processes are reasonably well understood, there are still significant issues with batch-to-batch variability which can lead to substantial issues in the downstream processing of the isolated material [16-18]. There exists significant potential to transform the entire industry by producing these products via continuous manufacturing. Continuous manufacturing has the potential for increases in efficiency, flexibility, and quality through the use of process analytical technology. Crystallization have been identified as key elements in improving manufacturing in the chemical and pharmaceutical industries [19].

There are two major areas that need to be researched for the conversion of batch processing to continuous. The first is to research ways to convert processes to continuous using existing technology. The second is to develop new technologies and techniques to perform these unit operations. Figure 1-1 shows a schematic of a current typical drug manufacturing process (top) and a proposed new method of manufacturing drugs (bottom).

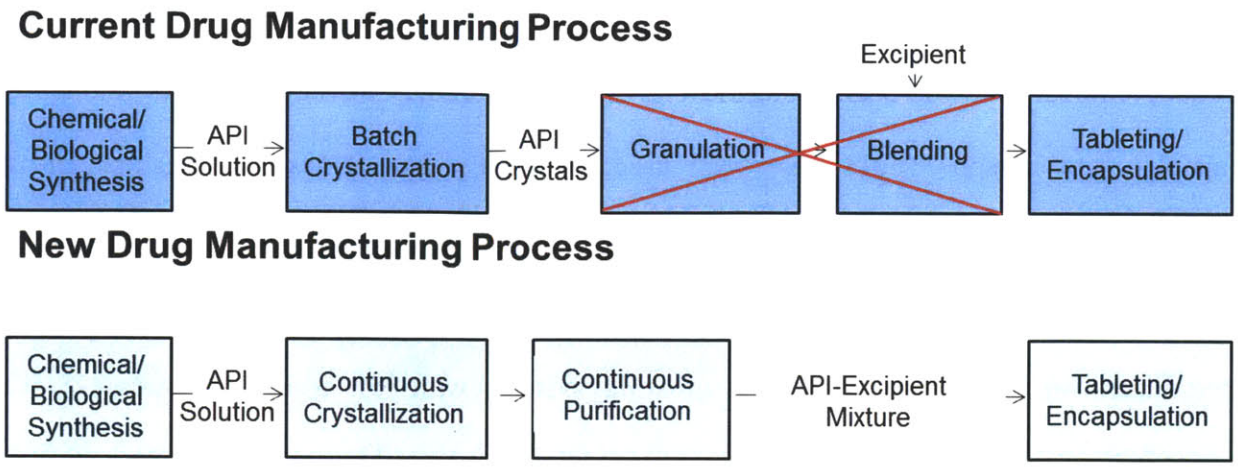

Figure 1-1: Flow chart of current and proposed drug manufacturing process

One major issue with continuous downstream processing is that performing unit operations with significant solids handling like continuous granulation, blending, and mixing can be difficult. In order to facilitate this process, removing these steps by performing crystallizations in which the final product is more amenable for downstream processing would be advantageous.

Both of these research projects have been studied and are presented in this thesis. Two continuous crystallizations processes were developed using existing MSMPR crystallizers. Additionally, evaporative emulsion crystallizations were performed to make spherical agglomerates for two purposes. The first aim was to make spherical agglomerates of excipients to use as surfaces for heterogeneous nucleation of API's. The second aim was to make composite spherical agglomerates which would be more amenable for direct processing.

1.3. Continuous Crystallization

The focus of the Novartis-MIT Center for Continuous Manufacturing is the development of new technologies that will allow continuous pharmaceutical manufacturing. One of the important milestones for the center has been the development of a demonstration unit for continuous manufacturing. This work describes the two continuous crystallizations that were developed as part of this demonstration unit.

The most common types of continuous crystallizers are mixed-suspension, mixed product-removal (MSMPR) and plug-flow crystallizers. Models for both types developed by Randolph and Larson (1971) have been used extensively by various investigators for the simultaneous determination of nucleation and growth kinetics in crystallization systems [7, 18, 20-23]. Both MSMPR and plug-flow crystallizers have their advantages, but plug-flow crystallizers are usually used for fast growing systems with low residence times [7]. The compounds used in this study are slow growing and thus have long residence times. For the system being studied, MSMPR crystallizers were found to be more appropriate. This paper investigates experimentally and through modeling the cascaded MSMPR multistage crystallization system developed to perform a continuous reactive crystallization.

Two different compounds were studied in this work. Both are crystallization steps from the manufacturing of Aliskiren Hemifumarate. Aliskiren Hemifumarate is a renin inhibitor approved for the treatment of hypertension. It was approved for sale by the FDA in 2007 and is sold under the trade names Tekturna and Rasilez. This API was chosen as the model compound because it was observed that there were many areas of the manufacturing process that could greatly benefit from switching from batch processing to continuous processing. One of the crystallizations studied is for an intermediate purification (Aliskiren boc-base), while the second crystallization is a simultaneous reaction and crystallization of the final active pharmaceutical ingredient (Aliskiren Hemifumarate). The batch processes for both of the crystallizations are highly complex with high throughput times. The continuous crystallization systems described herein are shown to significantly reduce the throughput time without compromising process yield or purity [24, 25].

1.4. Spherical agglomerates as surfaces for heterogeneous nucleation

One means for controlling such properties is through the use of heterogeneous nucleation. Heterogeneous nucleation is nucleation in the presence of a surface or an interface. It has been used in conjunction with organic crystals, polymers, and self-assembled monolayers (SAMs) to manipulate crystallographic orientation and to control the nucleation of different polymorphs [26-31]. Heterogeneous nucleation can also significantly increase nucleation rates. It has been shown that tuning specific chemistries on polymeric surfaces by modulating mesh sizes can change the induction time of aspirin by 4 orders of magnitude [32-34]. In another study, Form I of acetaminophen (AAP) crystallized in the presence of single crystals of α-lactose monohydrate and D-mannitol was shown to nucleate approximately five times faster than AAP nucleated from the bulk [35]. The reduction in induction time was due to a functional group match between AAP and lactose and mannitol rather than a purely geometric lattice match – the substrate and AAP having complementary functional groups allowed for significant hydrogen bonding at the interface. This was demonstrated by crystallizing AAP in the presence of graphite, whose (100) face shares a coincident lattice match with certain faces of Form I AAP. Although graphite decreased the induction time by a factor of 2 when compared to bulk nucleation, graphite was not as effective as α-lactose monohydrate or D-mannitol. These studies highlight the importance of considering both lattice matching and molecular functionality when designing heterogeneous crystallizations.

Although single crystal substrates have been shown to increase the nucleation rate of AAP, modifying the crystal morphology may further enhance nucleation kinetics. For example, Carter et al. [14] and Bonafede et al. [15] demonstrated how the presence of two contact planes reduces the activation barrier for nucleation more than just one contact plane. Exposing many additional

crystal faces through modulation of the crystal morphology could induce improved nucleation behavior. One method of fabricating substrates with modified morphologies is to crystallize them as spherical agglomerates. Spherical agglomerates of substrates tend to be composed of densely packed single crystals [36, 37]. Scanning electron microscope images from different studies have shown that spherical agglomerates have increased surface roughness compared with their corresponding single crystals, and may also exhibit differences in their morphologies [36-39].

In the present study, we have explored how crystallizing certain substrates as spherical agglomerates can alter their surface morphology which may lead to crystal faces being exposed that are not present in the equilibrium single crystal morphology. The effect that these differences in crystal morphology may have on heterogeneous nucleation kinetics was then explored. Spherical agglomerates of triclinic lactose and D-mannitol were crystallized using a previously developed evaporative water-in-oil emulsion technique [40]. The surface morphology and diffraction patterns of the agglomerates were characterized using image analysis and X-ray powder diffraction, respectively. If new peaks were present in the diffraction patterns of the agglomerates they were assigned miller indices by comparing them to peaks from calculated powder patterns. The effect of the morphology changes and newly available crystal faces on the induction time of AAP was then measured. Lattice matching software (EpiCalc) and molecular dynamics simulations were used to rationalize these effects in terms of epitaxial ordering and favorable interactions between the substrate and AAP. Finally, with the discovery of new lattice matches and chemistries on the surfaces of the agglomerates we are able to explain the differences between the nucleation behaviors [27, 41, 42].

1.5. Composite spherical agglomerates

In addition to enhancing nucleation kinetics, spherical particles or agglomerates have a number of physical properties that are beneficial for downstream processing. Some crystal morphologies such as needles can adversely affect the downstream operations of filtration, drying, and compression, and can also affect physical properties such as dissolution rate and solubility. Many earlier studies have shown that spherical agglomerates of API's are easier to filter, have better flowability, and often are more compatible for direct compression [36-38, 43, 44] than single crystals or powders. Much of the previous work on spherical crystallization or agglomeration was based on the use of a 3-solvent system to enact agglomeration of crystals, as described by Kawashima [39, 45-48]. Spherical particles of glycine have been made using evaporation from monodisperse microemulsions [49]. Spherical particles have also been obtained through the growth of crystalline agglomerates inside water-in-oil emulsion droplets through the slow evaporation of the droplets to generate supersaturation of the dissolved substance, allowing time for the nucleation and growth of these spherical agglomerates. This technique has been used to prepare spherical agglomerates of glycine and glutamic acid hydrochloride [40]. This approach did not work for all systems investigated, however; ephedrine hydrochloride, for instance, crystallized in the continuous phase rather than in the droplets. In other cases, nucleation occurred within the droplet, but as single crystals rather than as the desired spherical agglomerates of small crystallites with their better dissolution properties. It would be beneficial to develop a more robust, general method for generating spherical agglomerates to expand the range of API's to this approach for the enhancement of processing and physical properties may be applied; in this work, we show that heterogeneous nucleation within the confined droplets may be exploited to improve the spherical agglomeration process.

Heterogeneous nucleation is that which occurs in the presence of an interface or surface, which can affect nucleation behavior significantly [26, 27, 30, 31, 50], and not in the bulk solution. It has been shown that crystallization experiments performed in the presence of polymeric surfaces with various chemistries can reduce the induction time for the nucleation of aspirin and acetaminophen [32-34, 51]. In another study, acetaminophen crystals were shown to nucleate significantly faster in the presence of both lactose and mannitol than when nucleated homogeneously, attributed to extensive hydrogen bonding at these heterogeneous interfaces [35]. These studies demonstrate that by the selective choice of the surface and its properties, nucleation kinetics can be enhanced significantly. We show here that it is possible to use heterogeneous surfaces to modify the morphology of material crystallized inside emulsion droplets.

Glycine (as demonstrated before) and lactose were readily crystallized as spherical agglomerates and thus served as good heterosurfaces for the templating of D-Mannitol, sodium chloride, and potassium chloride, which were identified as good targets for morphology modification.. The resulting composite spherical agglomerates were characterized using multiple analytical techniques. This work demonstrated that water-in-oil crystallizations with heterosurfaces can be used to prepare spherical agglomerates of materials that otherwise would not crystallize as such.

2. EXPERIMENTAL

2.1. Materials

Mannitol, sodium chloride, potassium chloride, glycine, fumaric acid, dodecane, span 20, span 80, hexadecyltrimethylammonium bromide, ethyl acetate, and hexane (all 99% or higher) were purchased from Sigma Aldrich. α-Lactose monohydrate (99% pure) was purchased from Emprove. Ethanol (200 proof) was purchased from VWR International. Deionized water was produced using a Millipore Milli-Q system. Aliskiren lactone (C1), amino-dimethyl-propionamide, Aliskiren boc-base (C2), and Aliskiren free base (C3) were received from Novartis. The Aliskiren free base was received dissolved in ethanol, so in order to get it into a usable form, the ethanol was evaporated using a roto-vap, and the free base was re-suspended in ethyl acetate.

2.2. Analytical Techniques

Focused beam reflectance measurement [FBRM] was used to detect nucleation and to measure chord length distributions (CLD) of the solid product [52, 53]. The FBRM device was a Lasentec S400 probe from Mettler Toledo, with a measurement range from 785 nm to 1000 μm. X-ray powder diffraction (XRPD) patterns were recorded with a PANalytical X'Pert PRO Theta/Theta Powder X-ray Diffraction System with a Cu tube and X'Celerator high-speed detector. This technique was used to identify crystal forms, determine polymorphism, and analyze crystallinity. Differential Scanning Calorimetry (DSC) was used to analyze crystallinity of crystals and for compound identification. DSC measurements were performed using a Q5000 DSC from TA instrument.

Crystal morphology was observed by a Zeiss Axiovert 200 optical microscope in transmission mode with a differential interference contrast polarizer and magnification range from 5x to 50x. Prior to collection of Scanning Electronic Microscope (SEM) images with a JEOL 6060 SEM at a 5 kV operating voltage, the samples were sputter coated with a Quorum Technologies SC7640 high resolution gold/palladium sputter coater. Concentration and purity were measured using High Performance Liquid Chromatography (HPLC). Mother liquor samples were taken using PTFE syringe filters with 0.2 μL pore size. An HPLC instrument (Agilent Technologies 1200 Series) with a column Nucleosil 100-3 C18 (4.0 X 125 mm, 3 μm) was utilized for measuring the concentration at 230 nm, using an Agilent 1200 Series UV detector. Measuring conditions were flow rate: 1.0 mL/min, injection volume: 20 μL, and temperature: 50 °C.

2.3. Crystallization of Aliskiren Boc-base

Multistage continuous crystallization experiments were carried out in a self-assembled multistage crystallization system. Each stage was operated as a MSMPR crystallizer. The experimental system consisted of two 50 milliliter (mL) glass jacketed crystallizers with independent temperature control and overhead mechanical stirring. Feed solution containing C1 was continuously pumped into the first crystallizer using a peristaltic pump (flow rate range 0.006 - 600 mL/min, MasterFlex, provided by Cole-Parmer corporation). In this study, two different configurations were studied. In the first configuration – Configuration A – supersaturation was generated in the first vessel using cooling and supersaturation was generated in the second vessel using both cooling and anti-solvent addition. For Configuration B, supersaturation was generated in the first vessel using both anti-solvent and cooling, and the second vessel was cooled even further. Schematics of the experimental setup can be seen in

Figure 2-1. The suspension that was generated in the first crystallizer was transferred to the second stage using a peristaltic pump. The temperature of both vessels was controlled +/- 0.1°C with a NESLAB RTE Refrigerated Bath Circulator.

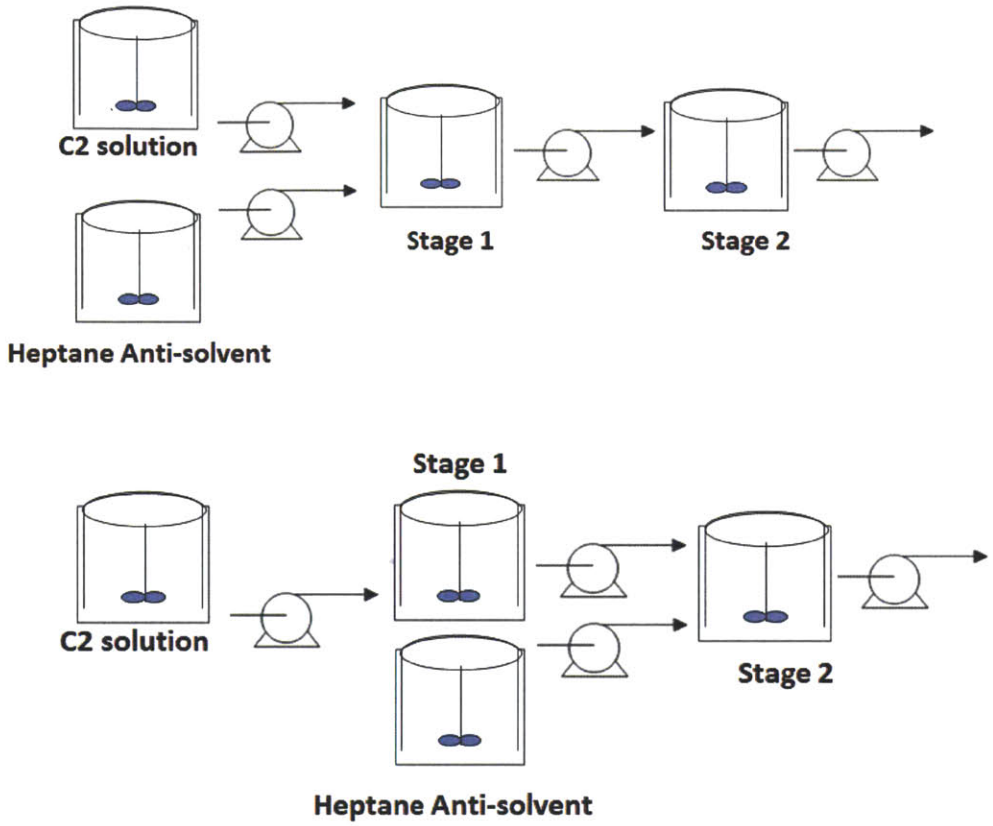

Figure 2-1: Schematic Diagram of Continuous Crystallization Apparatus for C2

The concentrations of C1 and C2 in the feed material and mother liquor were measured by high performance liquid chromatography (HPLC). Mother liquor samples were taken by filtering slurry samples from each vessel using PTFE syringe filter with 0.2 μL pore size.

Anti-solvent cooling continuous crystallization experiments for C2 were performed using the continuous crystallization apparatus described in Figure 2-1. The feed solution consisted of EtOAc with 13% (m/m) C2 at room temperature, 2% (m/m) C1, and 1% (m/m) impurities that were generated in the synthesis of C2. The feed solution was directly pumped into the first

crystallizer at a flow rate 0.125 mL/min. The working volume of the first stage was 30 mL and the residence time of each stage was set to 4 hours. The slurry in the first crystallizer was then pumped into the second crystallizer. Concurrently an anti-solvent stream of heptane was added to the vessel. The heptane flow rate was set such that it would comprise 25% (m/m) of the solvent mass (0.036 mL/min). The temperatures of Stages 1 and 2 were -5°C, and -10°C, respectively. The duration of the experiment was 33 hours (four total residence times). The concentration of the mother liquor and the chord length distribution were both monitored over time. Once the signals leveled out, steady state was reached.

2.4. Crystallization of Aliskiren Hemifumarate

A schematic of the continuous crystallization set-up used for experimentation can be seen in Figure 2-2. The system has two 50 mL mixed suspension mixed product removal (MSMPR) crystallizers in series. Each is jacketed for temperature control and has independent overhead stirring. Material is pumped into and out of each vessel using peristaltic pumps.

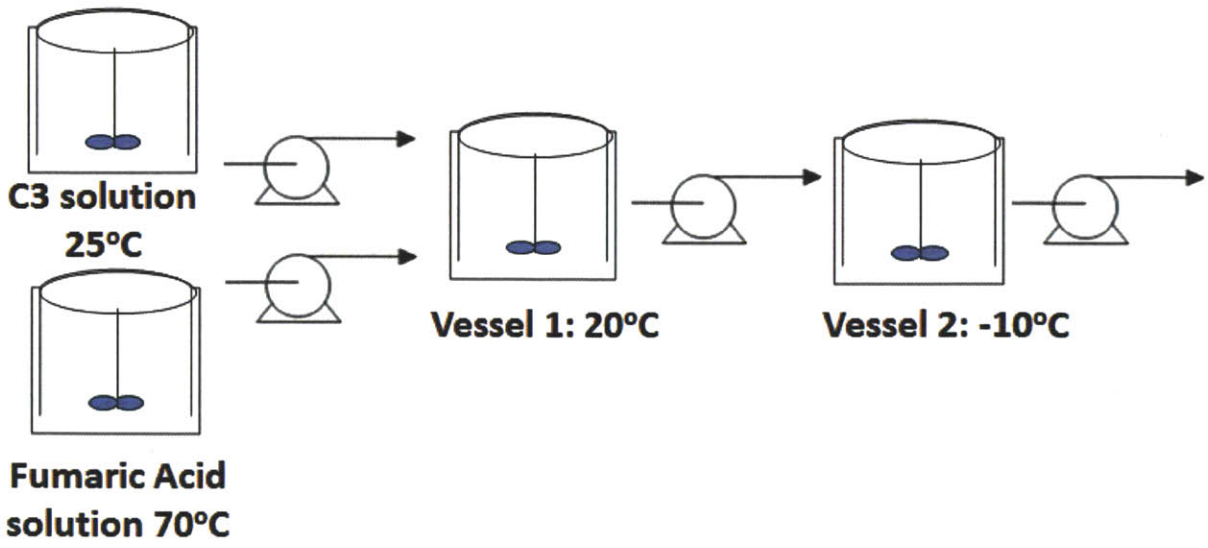

Figure 2-2: Continuous Crystallization Apparatus for Aliskiren Hemifumarate

In a typical experiment, ethyl acetate containing 6 w/w% Aliskiren free base was pumped into the first vessel. Concurrently, an ethyl acetate / ethanol solution (50/50 w/w%) containing 5 w/w% fumaric acid was also pumped into the first vessel. The C1 – ethyl acetate mixture is maintained at room temperature. The fumaric acid solution was kept separately at 70°C to solubilize the fumaric acid. A molar ratio of 0.58 moles fumaric acid to 1 mole free base was used to produce the hemifumarate salt. The slight excess was to ensure that all of the free base reacted with fumaric acid to form the hemifumarate. Though the free base is freely soluble in ethyl acetate, the hemifumarate salt is much less soluble and spontaneously nucleates. The temperature of the first stage of the crystallization is 20°C, and the slurry is then pumped into the second vessel which operates at -10°C. This second vessel is used for further nucleation and growth of the crystals. Each vessel has a 4 hours residence time. The temperature of each vessel was controlled to +/- 0.1°C with a NESLAB RTE Refrigerated Bath Circulator.

2.5. Equilibrium Impurity Distribution Coefficients

The distribution of the impurity between the solid and liquid phases at each stage of crystallization is determined by the Distribution Coefficient [8, 54], which can be also expressed as: [54]

$$DC_j = \frac{\left(M_{i,j} / M_{A,j}\right)}{\left(C_{i,j} / C_{A.j}\right)} \qquad (1)$$

A mass balance for the impurity over a stage j has terms for the impurity coming in ($C_{i,j-1}$, and $M_{i,j-1}$), a term for the impurity going out in solution ($C_{i,j}$), and a term for the impurity accumulated in the crystals ($M_{i,j}$)

$$C_{i,j-1} + M_{i,j-1} = C_{i,j} + M_{i,j} \qquad (2)$$

Where $C_{i,j-1}$, and $M_{i,j-1}$ are the concentrations of impurity in liquid and solid phase entering stage j, and $C_{i,j}$, and $M_{i,j}$ are the concentrations of impurity in liquid and solid phase leaving stage j.

From the experimental data shown in Figure 8, the Distribution Coefficient at each stage is a function of the concentration of impurity, which can be expressed as follows:

$$DC_j = a\left(\frac{C_{i,j}}{C_{i,j}+C_{A,j}}\right)+b \qquad (3)$$

Where a and b are experimental parameters.

Substituting equation (3) into (1) to eliminate DC_j, and substituting into (2) yields a quadratic expression, from which the concentration of impurity at stage j can be calculated:

$$C_{i,j}{}^2\left[-1-b\frac{M_{A,j}}{C_{A,j}}-a\frac{M_{A,j}}{C_{A,j}}\right]+C_{i,j}\left[C_{i,j-1}+M_{i,j-1}-C_{A,j}-bM_{A,j}\right]+\left[C_{A,j}\left(C_{i,j-1}+M_{i,j-1}\right)\right]=0 \qquad (4)$$

Finally, purity of the host compound is calculated as the mass faction of the host in the solid phase

$$Purity(\%) = \frac{Mass\ of\ Product}{(Mass\ of\ Product + Mass\ of\ impurity)} \qquad (5)$$

In order to measure distribution coefficients, a sequence of crystallization experiments was carried out. For the C1 crystallization, a series of anti-solvent and cooling crystallization experiments was performed. Heptane was added to a saturated solution of C1 in EtOAc at 25°C in increments of 5% heptane by mass up to a total of 25% heptane. The solution was then cooled to -10°C in increments of 5°C. For C3, sufficient fumaric acid was added to react completely with the freebase at 25°C, and cooling crystallization experiments were subsequently performed in 5°C increments down to -10°C. After each of these crystallization experiments, the crystallized solids were separated by filtration and dried overnight. Samples of solids and mother liquor were analyzed by HPLC to determine distribution coefficients.

When impurities incorporate at small level into the crystal, the incorporation can be characterized by a distribution coefficient which is defined as the ratio of impurity concentrations to the host compound concentration in the solid phase divided by that ratio in the liquid phase.

2.6. Population Balance Modeling

Final crystal properties including yield, purity, morphology, and particle size are important for the success of a crystallization process. A model relating nucleation and crystal growth kinetics to operating variables is necessary to evaluate the effect of operating conditions on all of these properties. A model of the continuous crystallization process based on the simultaneous solution of the Population Balance Equation (PBE) and Mass Balance Equation has been developed [8]. The purpose of the model is to predict the crystal purity, yield, and size distribution of the crystals obtained in the multistage cascaded continuous crystallization system [13, 18, 21, 55, 56]. FBRM was employed to determine the particle size distribution for the parameter estimation of the model in the current work. The crystals from both of the crystallization processes described have needle-like morphology. Because FBRM does not directly measure the particle size distribution, the particle size distributions from the model and experimental were not precisely the same [13, 21]. Thus, the fitted growth and nucleation parameters are not exactly correct values. The model, however, is still useful tool to study the effects of operating conditions on the purity and yield. Other published work has used CLD measurements from FBRM directly in modeling rather than converting it to a particle size distribution first [8, 57, 58]. Equilibrium distribution coefficients were also included in the model to give information about crystal purity.

Assuming a clear feed stream into the first stage, the general population balance equations can be reduced to

$$G_1\tau_1\frac{dn_1}{dL}+n_1=0 \tag{6}$$

$$G_2\tau_2\frac{dn_2}{dL}+n_2=n_1 \tag{7}$$

Where L is the characteristic size of the crystal, $n(L)$ is the number density of crystals per unit volume of size between L and L+dL, G is the size-independent crystal growth rate, and τ is the mean residence time. These equations can be solved analytically using the boundary condition: $n(0)=n^0$, where n^0 is the crystal density of zero size nuclei. The analytical solution is

$$n_1=n_1^0\exp\left(\frac{-L}{G_1\tau_1}\right) \tag{8}$$

$$n_2=n_2^0\exp\left(\frac{-L}{G_2\tau_2}\right)+n_1^0\left[\frac{G_1\tau_1}{G_1\tau_1-G_2\tau_2}\right]\left[\exp\left(\frac{-L}{G_1\tau_1}\right)-\exp\left(\frac{-L}{G_2\tau_2}\right)\right] \tag{9}$$

The rate at which solute is lost from the solution phase is equal to the rate at which mass is gained by the solid phase. Thus, a mass balance on the solute crystallized in each stage gives:

$C_0 = C_1 + M_{T1}$ for stage 1,

And, $C_1 = C_2 + M_{T2}$ for stage 2,

where C_0, C_1, C_2 are the solute concentration at feed, stage 1, and 2 respectively, and M_{T1}, M_{T2} are the suspension densities at stage 1 and 2, which are calculated from the third moment of the population density at each stage.

$$M_{T1}=\int k_v\rho L^3 n_1 dL=6k_v\rho\, n_1^0(G_1\tau_1)^4 \tag{10}$$

$$M_{T2} = 6k_v\rho\left\{n_2^0(G_2\tau_2)^4 + n_1^0\left[\frac{G_1\tau_1}{G_1\tau_1 - G_2\tau_2}\right]\left[(G_1\tau_1)^4 - (G_2\tau_2)^4\right]\right\} \quad (11)$$

where ρ is the solid density and k_v is a volume shape factor.

The crystal growth rate and nucleation rate can be expressed as a function of supersaturation in the form of empirical power-law equations (8), (9), and (10), where G_i and B_i are crystal growth rate and nucleation rate at stage i respectively, C_i is the steady state concentration at stage i, C_i^{sat} is the equilibrium concentration at stage i, T is the temperature, R is the gas constant (8.314 J/mol·K), whereas k_g, k_{g0}, k_{g1}, g, k_b, and b are model parameters.

$$G_i = k_g\left(\frac{C_i - C_i^{sat}}{C_i^{sat}}\right)^g \quad (12)$$

$$k_g = k_{g0}\exp\left(-\frac{k_{g1}}{R(T+273)}\right) \quad (13)$$

$$B_i = k_b\left(\frac{C_i - C_i^{sat}}{C_i^{sat}}\right)^b \quad (14)$$

$$n_i^0 = \frac{B_i}{G_i} \quad (15)$$

Temperature-dependent solubilities of Aliskiren Hemifumarate in EtOAc/EtOH were measured by HPLC.

Volume based distribution of the steady state CSD experimental data were converted to population density data using the relationship

$$n_{exp} = \frac{\Delta M\, M_T}{\Delta L k_v \rho L^3} \quad (16)$$

Where n_{exp} is the experimental population density, ΔM is the mass based CSD (%), M_T is the slurry density, ΔL is the size range, k_v is the volume shape factor, L is the characteristic size of the crystal and ρ is the crystal density.

If the error is defined as the difference between the measured (experimental) and calculated values of the crystal size distribution, then a least-squares optimization procedure to estimate the kinetic parameters consists of finding the values of θ that minimize the objective function $\psi(\theta)$ defined as the sum of squares of the error, where θ is the vector of model parameters, $\theta = [\ k_{g0},\ k_{g1},\ g,\ k_b,\ b\ ]$. The optimization problem is expressed as

$$\min_{\theta} \quad \Phi(\theta) = \sum_{1}^{\#stages} \sum_{0}^{L\max} \left[\left(n_{exp} - n(L) \right)^2 \right] \tag{17}$$

subject to equations (4) to (10).

Thus, the population balance equations for each stage, as well as the mass balances and expressions for kinetics of crystallization are solved with initial values for the parameters θ, and the obtained crystal size distribution for each stage is compared to the experimental data. The value of the parameters θ is then recalculated and the procedure is repeated until a minimum value for the sum of squares of the error is found. Typical assumptions include that the errors of each measurement are independent and are normally distributed with zero mean.

Once the optimal values for kinetics parameters are found, the crystal growth rates and nucleation rate at steady state are calculated for each stage, using equations (8), (9), and (10). The mass based mean size of the crystals can be estimated for each stage i from the third and fourth moments of the size distribution.

$$\left(L_{4,3}\right)_i = \frac{\int_0^\infty L^4 n_i \, dL}{\int_0^\infty L^3 n_i \, dL} \tag{18}$$

Using the population density expressions for each stage (equations (4) to (5)) to solve the integrals, crystal mean size is obtained as a function of mean residence times, crystal growth rate, and population density of nuclei for each stage.

$$L_{4,3} = 4G_1\tau_1 \tag{19}$$

$$L_{4,3} = \frac{4n_2^0(G_2\tau_2)^5 + \left[\frac{4n_1^0 G_1\tau_1}{G_1\tau_1 - G_2\tau_2}\right]\left[(G_1\tau_1)^5 - (G_2\tau_2)^5\right]}{n_2^0(G_2\tau_2)^4 + \left[\frac{n_1^0 G_1\tau_1}{G_1\tau_1 - G_2\tau_2}\right]\left[(G_1\tau_1)^4 - (G_2\tau_2)^4\right]} \tag{20}$$

2.7. Spherical Particle Generation

Spherical agglomerates were generated by evaporative crystallization from water-in-oil emulsions [40]. The lactose or D-mannitol was dissolved in 8 mL of water. The mass of each compound depended on its respective solubility at 40°C (0.25 g/mL lactose, 0.46 g/mL for D-mannitol). The aqueous solution (the dispersed phase) was then added to 72 mL of dodecane which served as the continuous phase. The mixture was stirred at 650 rpm at 70°C to obtain a stable emulsion. The emulsion was stabilized using 1 w/w% surfactant, a mixture of span 20 and span 80 at a mass ratio of 3 to 7. CTAB was added as an additive to promote nucleation in the emulsion system. Once the emulsion was stabilized (observed optically), the temperature was raised to 80°C to slowly evaporate the water. Samples were taken and analysed by optical microscopy every 15 minutes to determine when crystallization was complete. Once crystallization was observed, the particles were filtered and dried in a vacuum oven.

2.8. Nucleation Kinetics Measurements

Average nucleation induction time, τ, was measured to determine the effect of spherical morphology on the nucleation rate of AAP. The induction time is the time lag between the onset of supersaturation and the occurrence of nucleation. τ is a useful measure of how much a surface aids nucleation because the value can be greatly reduced if the surface lowers the kinetic barrier to nucleation [32]. Due to the stochastic nature of nucleation, a large number of identical experiments were required in order to obtain a statistically significant result. Several assumptions were made for this analysis. First, the detection of heterogeneous nucleation was the detection of secondary nucleation of AAP – it was assumed the time between heterogeneous nucleation and secondary nucleation occurring was negligible. Second, the time required for the system to reach the desired supersaturation was assumed negligible in comparison to τ. Finally, the growth rate of acetaminophen was assumed to be much faster than the nucleation rate, such that the time difference between nucleation and detection could be ignored.

Induction time data were collected using a RS10 Clarity Solubility Station from Thermo Fisher Scientific [59]. This method has been used in a number of other studies [33, 34]. A stock solution of AAP in ethanol was prepared (232.75 g/kg, saturated at 30°C). 1.5 mL aliquots were then syringe filtered into an HPLC vial to remove any solid impurities. The vials were agitated with a magnetic stir bar rotating at 700 rpm. The samples were then quench cooled to 15°C which resulted in a supersaturation (σ) of 1.36. $\sigma = c^*/c_{eq}$, where c^* is the actual concentration and c_{eq} is the equilibrium concentration at a given temperature. For experiments with the substrates, approximately 3 mg was added into each vial prior to the addition of the AAP/ethanol solution.

2.9. EpiCalc Calculations

The interface between a substrate crystal face and an overlayer crystal face is defined by 7 parameters: a_1, a_2, α (describing the substrate), b_1, b_2, β, (describing the overlayer), and ϕ. These parameters are shown in Figure 1. The parameters (a_1, a_2) and (b_1, b_2) are pairs of vectors describing the 2-dimensional lattices of a crystal substrate and overlayer, respectively. The parameters α and β are the angles between each pair of vectors. The variable ϕ is known as the azimuthal angle and is defined as the angle between the a_1 and b_1 vectors and therefore describes the orientation of the overlayer with respect to the substrate. The three modes of epitaxy are commensurism, coincidence, and incommensurism. Commensurism is defined as a total lattice match between the substrate and overlayer, while coincidence is a partial lattice match. Incommensurism means that the lattices do not match.

The lattice agreement between the substrate and AAP was determined using EpiCalc Version 5 [60-62]. This software calculates the lattice agreement between two surfaces using a dimensionless potential energy, V/V_0, as a measure of goodness of fit. The value for V/V_o ranges between –0.5 and 1, where a value of 1 indicates incommensurism, 0.5 implies coincidence, 0 indicates commensurism on a non-hexagonal substrate, and –0.5 commensurism on a hexagonal substrate. The angle ϕ was varied between 0° and 180° in intervals of 0.25°. The size of the overlayer was set to $25b_1 \times 25b_2$. The output is a plot of the potential V/V_o as a function of the azimuthal angle ϕ.

2.10. Molecular Dynamics Simulations

Systems containing a crystal slab of triclinic lactose or β-mannitol, with dimensions of approximately 90×90×15 Å, and an overlayer of AAP (Form I), with dimensions of

approximately 50×50×20 Å, were constructed with various crystal faces aligned to one another. The following faces of lactose and AAP were aligned: (140)/(001), (14$\bar{1}$)/(001), (20$\bar{1}$)/(001), (011)/(001), and (011)/(111). These faces were chosen as representative pairs in the absence of experimental data showing which faces of lactose and AAP are bound together. The (140), (14$\bar{1}$) and (20$\bar{1}$) faces of lactose were chosen because of their increased presence in the spherical agglomerates (*vide infra*) whereas the (011) face was chosen because it is the most abundant face in the single crystal form. The (001) and (111) faces of AAP were chosen because they have been previously determined to be the fastest growing faces [63]. For D-mannitol and AAP a previous epitaxy study demonstrated that the (00$\bar{1}$)/(100) are bound together, therefore we simulated the energy interaction between this pair [35]. Table 2-1 summarizes additional simulated pairings. These additional face pairings showed neither lattice matching from the EpiCalc calculations nor favourable energy interactions and will not be discussed in the results section.

Table 2-1: Face Pairings Between AAP and Lactose and Mannitol Investigated Using Molecular Dynamics Simulations in the Present Study.

		AAP			
		001	111	100	0$\bar{1}$1
Lactose	14$\bar{1}$	×			
	140	×			
	20$\bar{1}$	×			
	11$\bar{1}$	×	×		
	011	×	×		
	0$\bar{1}$1				×
	10$\bar{1}$	×	×		
Mannitol	00$\bar{1}$	×	×	×	

Each alignment was carried out such that the face-to-face distance between lactose or mannitol and the AAP overlayer was approximately 3 Å. After the initial alignment, the AAP overlayer was rotated through 2.5 degree increments for 360 degrees to produce 144 starting structures for each system. Following the rotations, all systems were placed in a period box with box vectors matching the b_1b_2-dimensions of the lactose/mannitol crystal. The b_3-direction on the other hand was ascribed a length of 120 Å so that face-to-face interactions of periodic images would be minimized. The basic system setup and geometric parameters are shown in Figure 2-3.

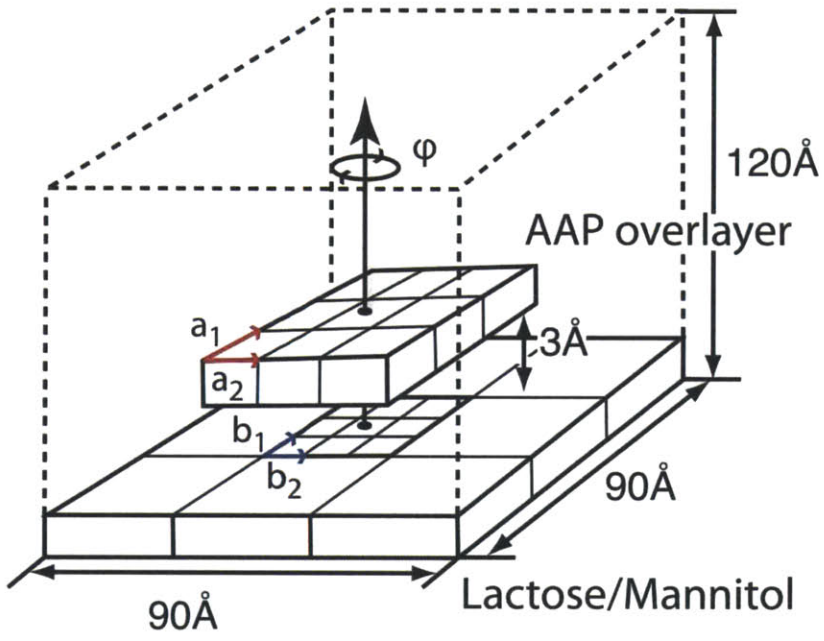

Figure 2-3: Crystal slabs of lactose and mannitol with overlayers of AAP were simulated using the basic geometries shown. The potential energy as a function of azimuthal angle (Φ) between crystal vectors a1 and b1 were produced by averaging energies from short low-temperature molecular dynamics simulations.

The Glycam06 force-field parameters [64] were applied to molecules in the lactose crystal, whereas the following procedure was used to derive parameters for AAP and D-mannitol: First, *xyz* coordinates of AAP and mannitol monomers were taken from the crystal structures of AAP (Form I) and the β polymorph of D-mannitol. The coordinates of these structures were relaxed to a local minimum on the potential energy surface (zero-imaginary frequencies) using

the B3-LYP/6-31G(d) level of theory. The electrostatic potentials (ESP) of the AAP and mannitol monomers were derived by carrying out a single-point energy calculation on the resultant structures with the HF/6-31G(d) level of theory. The resultant ESPs were fit using the RESP procedure [65, 66] to derive partial atomic charges in accordance with standard parameter development of AMBER-style force-fields [67]. The remaining parameters for describing bond, angle, dihedral and vdW potentials were taken from the generalized amber force-field (GAFF) [68]. All molecular dynamics simulations were carried out using the GROMACS 4.5.3 molecular dynamics suite of programs [69] by using the porting procedure of Sorin and Pande [70]. All quantum chemistry calculations were carried out using the Gaussian 03 program package [71].

7000 steps of steepest descent minimization on all rotamers were carried out to derive relative interaction energies (ΔE) as a function of azimuthal angle. The resultant structures were used as shooting points for 10 short (6 ps) low temperature molecular dynamics simulations. These simulations were performed in order to overcome local energy barriers without causing major disruptions of the relative lattice angles between the lactose and mannitol crystals and the AAP overlayer. The final structures from the MD simulations were optimized for a further 7000 steps of steepest descent minimization and the average potential energy of the 10 optimizations was taken as the energy for the given lactose/mannitol and AAP rotamer. All molecular dynamics simulations were coupled to a Berendsen thermostat and semi-isotropic Berendsen barostat to a target temperature of 100 K and target pressure of 1 bar. The isothermal compressibility in the *z*-direction was set to 0.0 bar^{-1} in order to maintain the large face-to-face separations between periodic images. Electrostatic interactions were calculated with the Ewald particle mesh method [72] using a real space cutoff of 20 Å. Bonds involving hydrogen atoms

were constrained using the LINCS algorithm [73] and the time integration step was set to 2 fs. A geometric definition for the existence of a hydrogen bond was used for the hydrogen bond analysis. The acceptor–donor distance cutoff was set to 3.5 Å. The angular acceptor– hydrogen–donor cutoff was set to 30°.

2.11. Composite spherical agglomerate generation

To form the composite spherical particles, the two components were dissolved together in water with concentrations set such that the template molecule would crystallize first, allowing the target to nucleate heterogeneously on the crystalline template surface. The concentrations were set such that the nucleation induction time for the template molecule was always shorter than that of the target molecule, as verified by experiments conducted on the individual components alone, in the absence of one another. A schematic of this process can be seen in Figure 2-4.

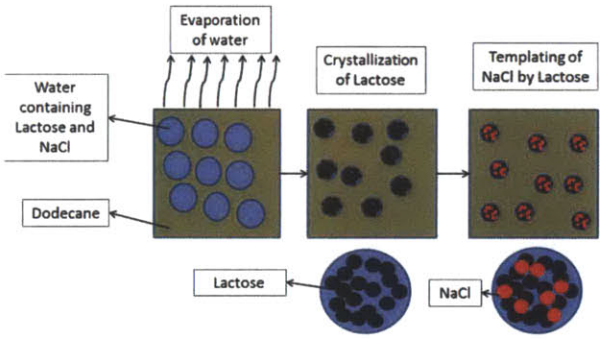

Figure 2-4: Schematic of composite spherical agglomerate generation. Emulsion of water containing heterosurface (lactose) and template (NaCl) is placed into dodecane and stirred. Emulsion is heated to evaporate water. The heterosurface crystallizes first, templating nucleation of the target molecule.

3. CRYSTALLIZATION OF ALISKIREN BOC-BASE

3.1. Introduction

This chapter describes the first of two continuous crystallization processes that were developed as part of the bench scale unit for continuous manufacturing. Each of the crystallizations had its own unique challenges. As an intermediate purification crystallization, the primary concerns for the crystallization of Aliskiren boc-base were purity and process yield. This chapter describes the work that went into the process development, including challenges using synthesized material rather pure starting material and the decisions that were made about where to add anti-solvent into the process. Additionally, this chapter describes the results of the process modeling performed on the crystallization system. This combined population and mass balance model was both fitted and validated using experimental data.

3.2. Process Development

3.2.1. Influence of water on the crystallization process of C1.

The feed solution to the crystallization consisted primarily of C1 and C2 in Ethyl Acetate. Crystallization experiments using pure ethyl acetate, C1 and C2 to form the starting solution resulted in a yield of 92% C1 recovered with greater than 98 % purity. Crystallization using feed material from an actual reaction (as opposed to using pure materials) gave a yield of 62% with significantly lower purity.

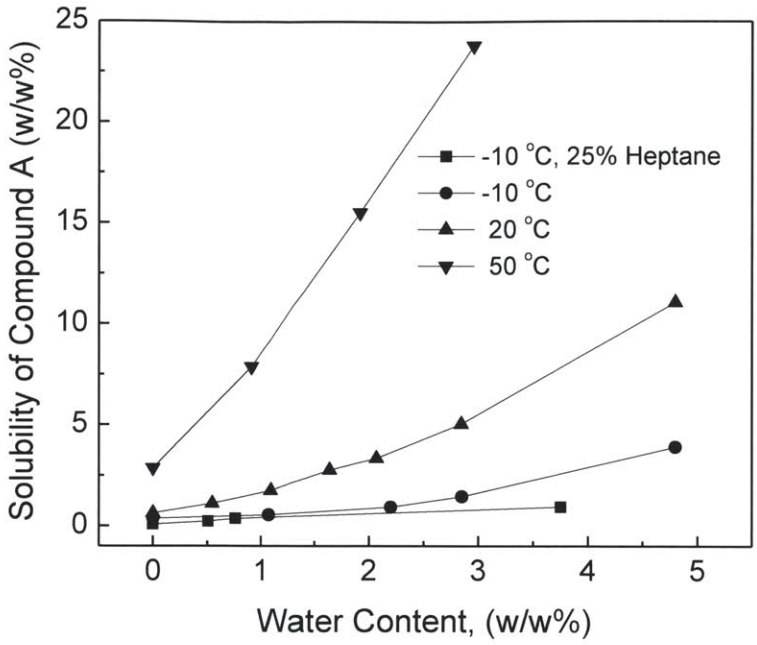

Figure 3-1: C1 solubility versus water content in the organic phase v

A review of the reaction and workup steps suggested that because of an upstream liquid-liquid separation step, nearly 5 % water was being entrained in the organic stream. The effect of water on the solubility of C1 can be seen in Figure 3-1. The presence of water significantly increased the solubility of C1 at all measured temperatures. This was unexpected as C1 has low solubility in both pure Ethyl Acetate and pure water, but a higher solubility in the mixed solvent.

A secondary solvent screen was undertaken to identify a suitable anti-solvent to improve the crystallization yield. Heptane was identified as a promising choice for the anti-solvent system. With the addition of heptane, the solubility of C1 was significantly reduced. From Figure 3-1, it can be seen that the addition of 25% heptane reduced the solubility of C1 at all water content levels. At 3.5 % water, adding 25% heptane reduced the solubility of C1 to below 0.9%, compared to around 2.5% for the solution without heptane. The solubility of C1 became stable with respect to increasing heptane content at 25% heptane solvent content. In consideration of

the working volume increase and the C1 concentration decrease with the addition of heptane, the heptane content was set at 25 (m/m) % of the total solvent.

Based on the above results, we employed a continuous anti-solvent + cooling procedure for the C1 crystallization with the temperature of the first crystallizer set at -5 °C and the second stage, was set at -10 °C.

3.2.2. Influence of anti-solvent on crystal properties.

To investigate the influence of anti-solvent on crystal properties, X-ray diffraction patterns of C1 crystallized with varying heptane concentrations were measured and the results are shown in the Figure 3-2. As the concentration of the anti-solvent was increased, the level of supersaturation also increased. The supersaturation increase lead to a higher nucleation rate and thus more fines and amorphous material in the final product. These are identified by peak broadening and a raised baseline of the diffraction patterns. From optical microscope picture as shown in Figure 3-3, it can be seen there are some large agglomerates in the crystals generated using 25 % anti-solvent.

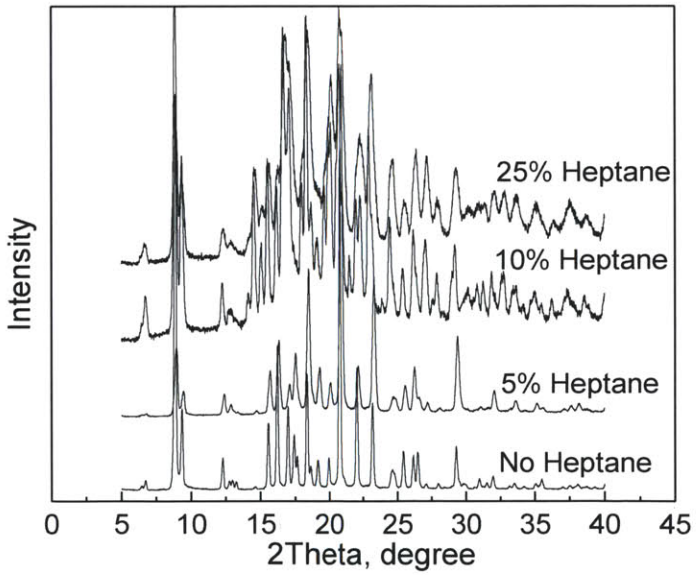

Figure 3-2: X-ray diffraction of C1 crystallized in EtOAc with different heptane content

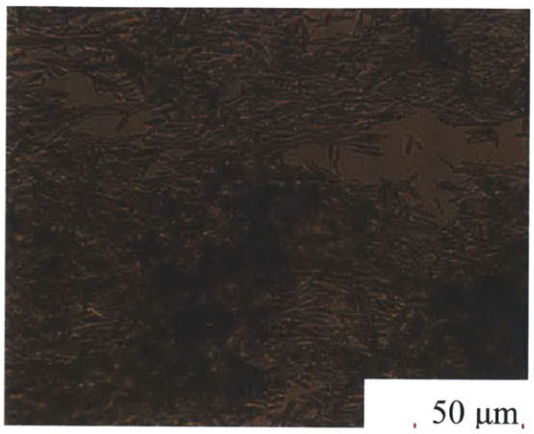

Figure 3-3: Microscope images of C1 crystallized in batch with 25% heptane

During the process development, it was not initially clear whether adding the anti-solvent in the first or the second vessel was a better option due to the unknown kinetic information. To answer which option will be better, the effect of the anti-solvent addition on the crystal properties was determined.

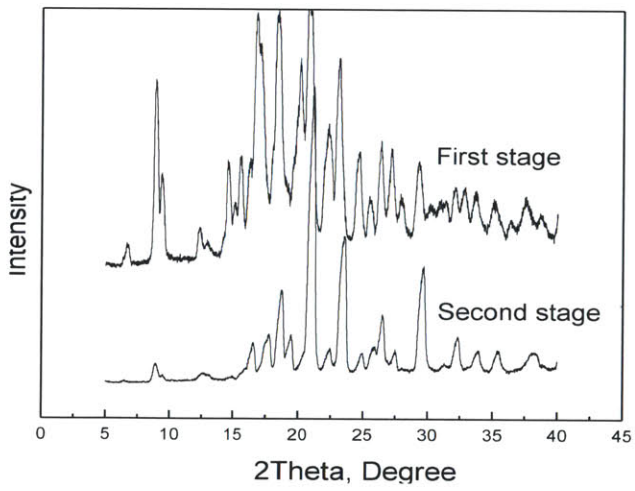

Figure 3-4: XRPD of C1 crystallized with anti-solvent feeding at the first stage

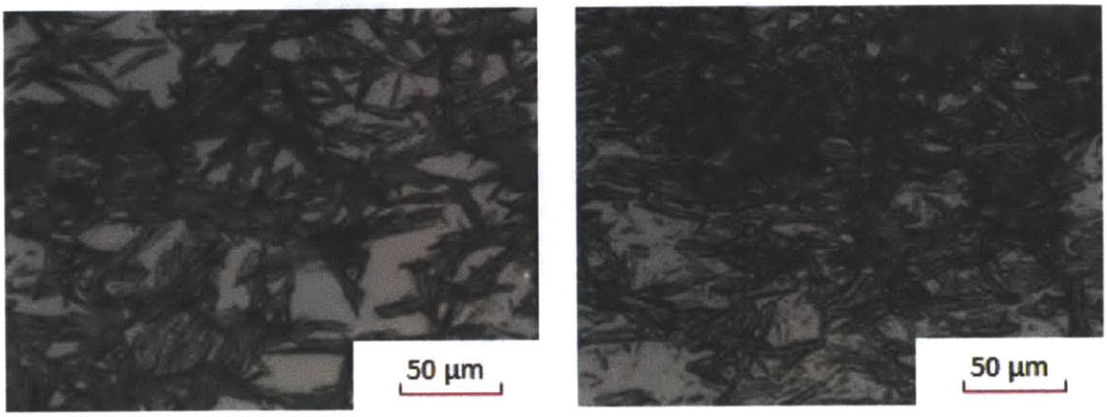

Figure 3-5: Microscope images of C1 with anti-solvent feeding at the first stage

The XRD patterns and optical microscope pictures for crystals generated with anti-solvent feeding in the first stage can be seen in Figure 3-4 and 3-5, respectively. Figures 3-6 and 3-7 contain XRD and optical microscope pictures for crystals generated with anti-solvent added into the second vessel.

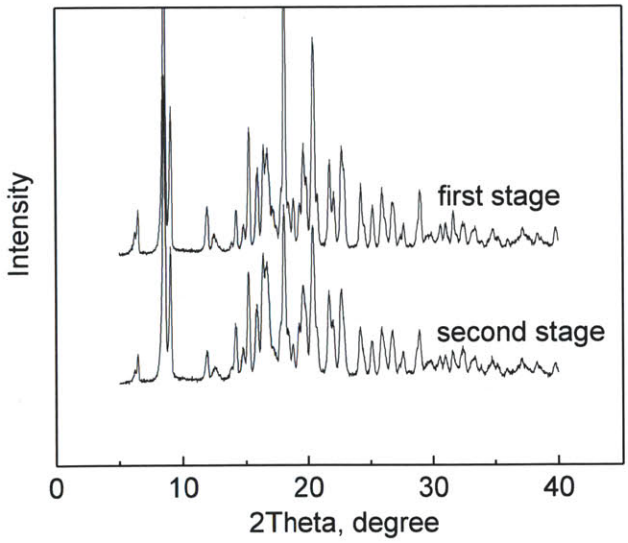

Figure 3-6: XRPD of C2 crystallized with anti-solvent feeding at the second stage

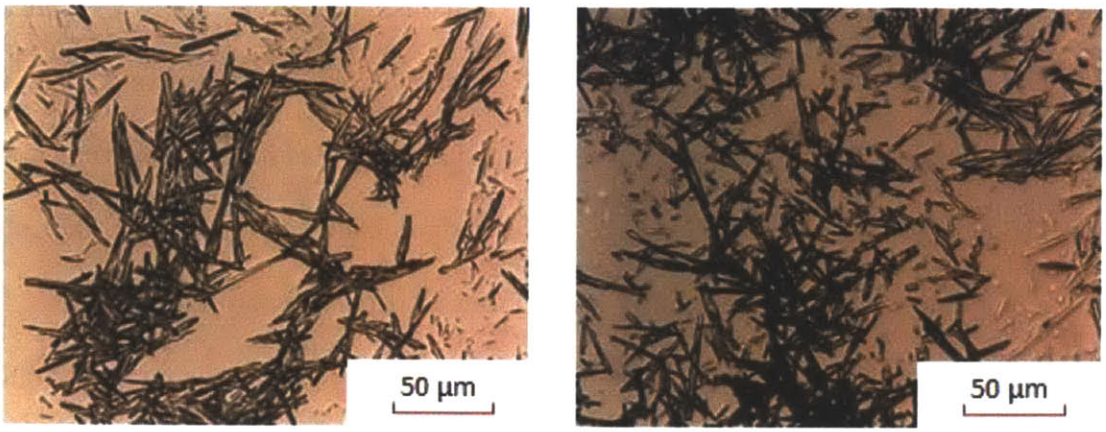

Figure 3-7: Microscope images of C1 with anti-solvent feeding at the second stage

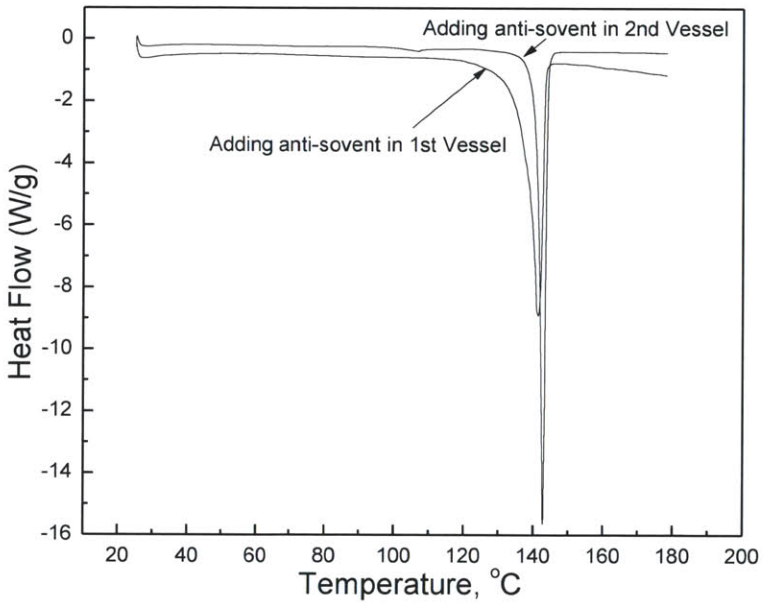

Figure 3-8: Comparison of DSC curves of the final products of C1 crystallization

The crystals generated with anti-solvent feeding at the second stage have better crystallinity compared to those generated with anti-solvent feeding at the first stage. Comparing the X-ray patterns in Figures 3-4 and 3-6, the crystals from the continuous process with anti-solvent feeding at the second stage have a much stronger baseline with much sharper and

narrower peaks. DSC curves shown in Figure 3-8 help demonstrate this crystallinity result. As shown in the DSC curves, for the product generated by adding anti-solvent in second stage, the melting peak is sharper and narrower and thus more crystalline. By adding anti-solvent in the second stage, the supersaturation in the first stage vessel is significantly decreased, and the entire process was operated at lower supersaturation level. From the optical microscope pictures, the crystals generated with anti-solvent added in the first vessel are much more agglomerated. Crystals generated with anti-solvent added to the second vessel are more suitable for downstream processing because they allow for an easier downstream filtration step.

3.2.3. Evolution of continuous crystallization process.

The temperature, yield of crystallization and the CLD of the crystals in the two stages were tracked over the duration of crystallization process to monitor the process state to confirm that steady state was reached. As shown in Figure 3-9, the temperature in each stabilized after 1-2 residence times. Initially, no temperature was recorded until the level of slurry reached the temperature probes.

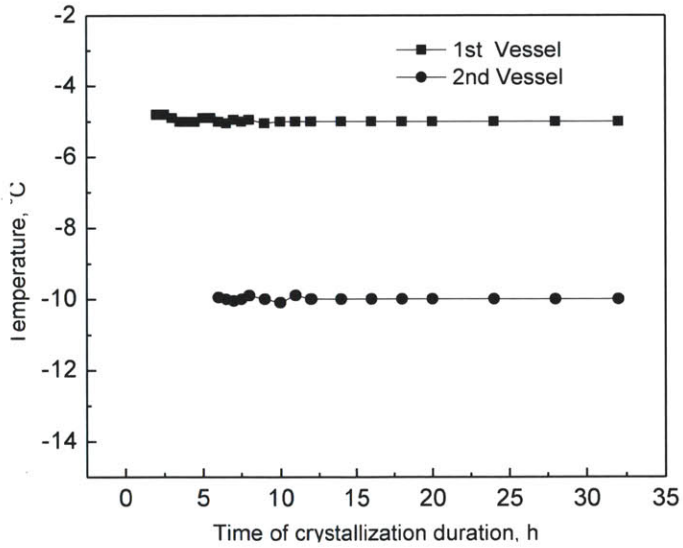

Figure 3-9: Temperature versus time in the two stages

The concentration of C1 in the mother liquor and the CLD of both of the two stages were tracked over the duration of the crystallization process. As shown in Figure 3-10, the yield stabilized after 3 residence times. From Figures 3-11 and 3-12, the CLD also stabilized after 3 residence times. As shown in those figures, after 3-4 residence times, the variables monitored were consistent, and indicate that the steady state was reached.

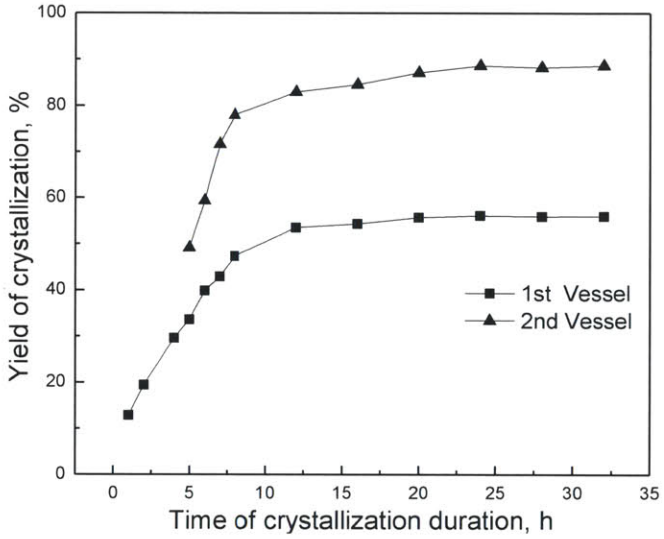

Figure 3-10: Yield evolution in the two stages during crystallization startup

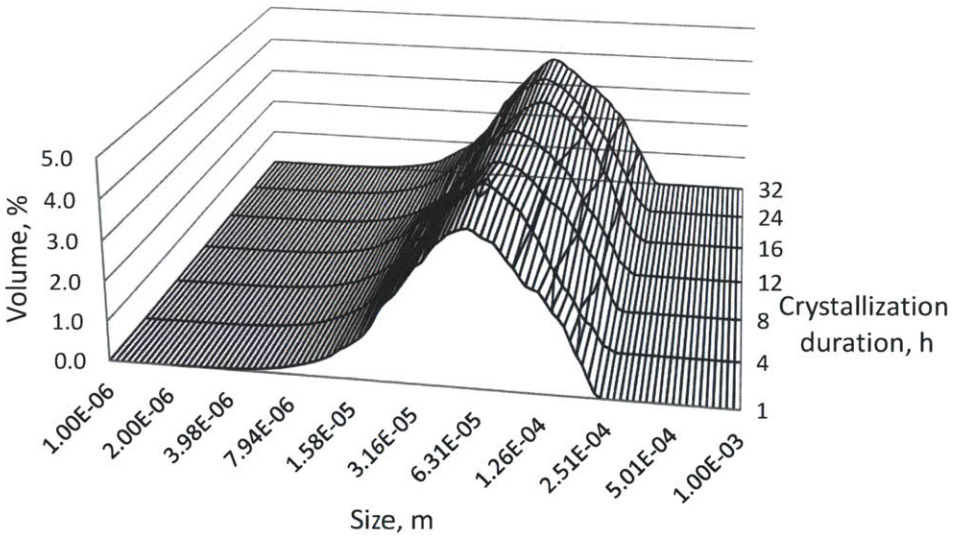

Figure 3-11: CLD evolution in first stage

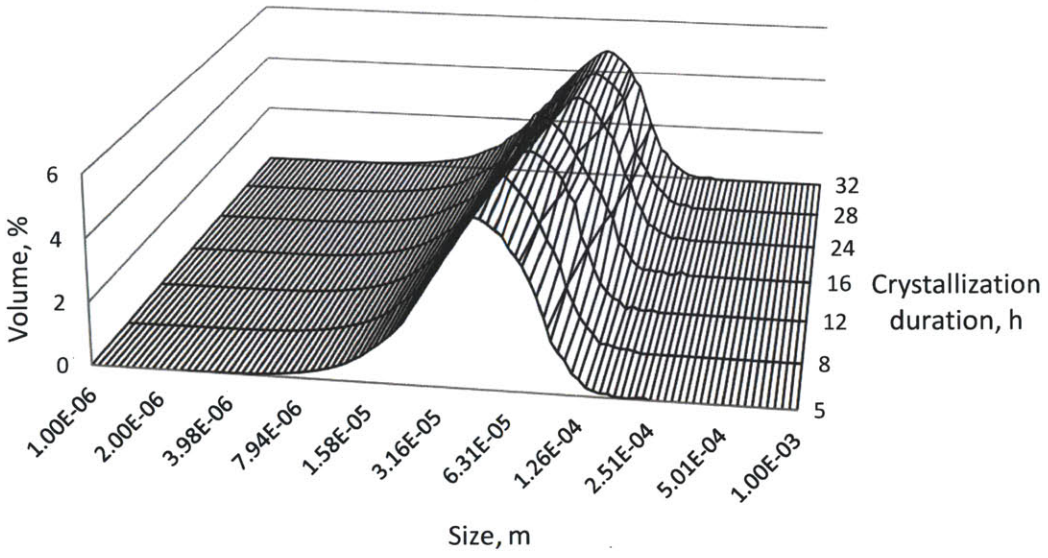

Figure 3-12: CLD evolution in second stage

To determine if there was significant classification in the crystallizers, samples were taken at different locations in second stage, including the top of the crystallizer, the bulk slurry and the bottom of the crystallizer. No significant difference was observed as shown in the microscope images in Figure 3-13.

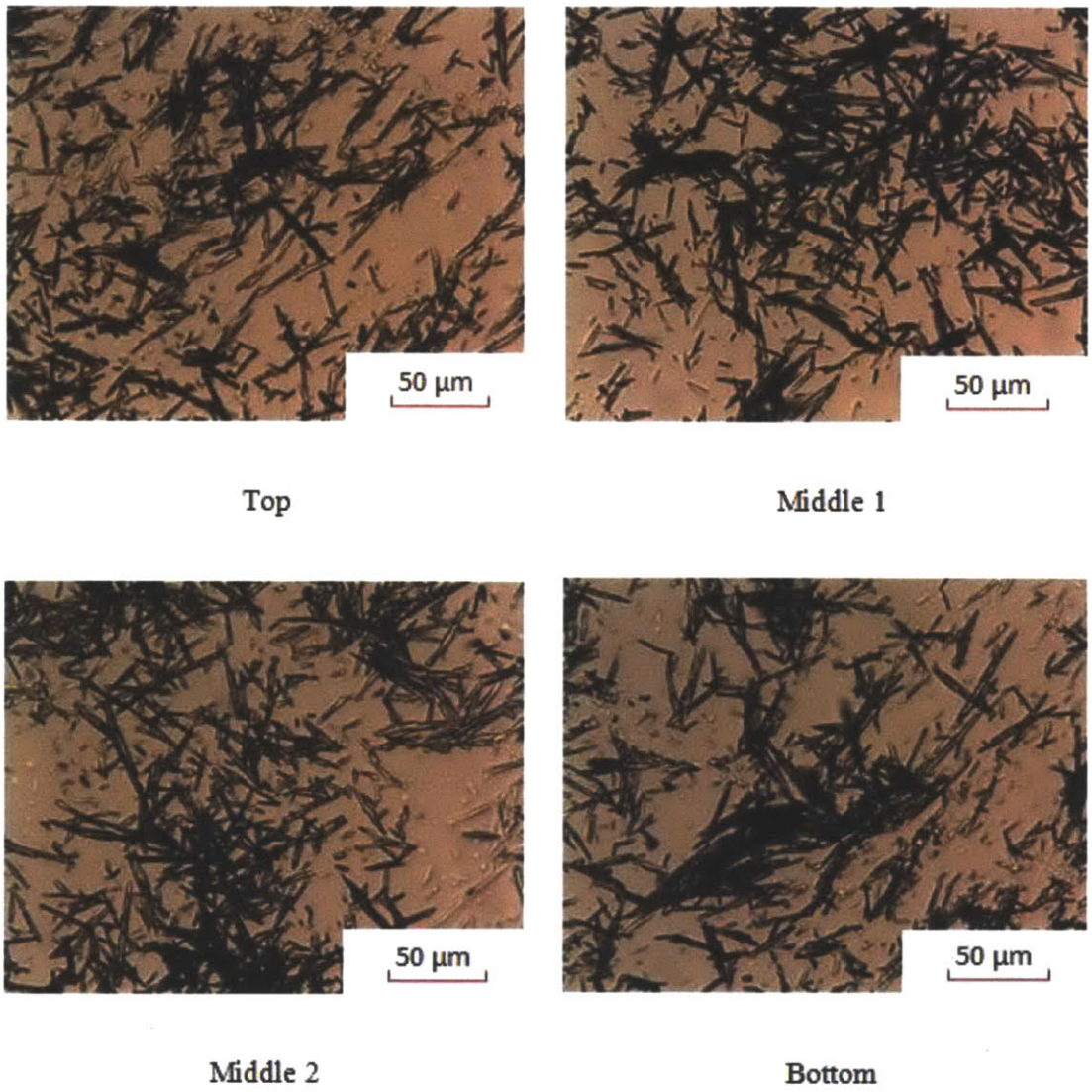

Figure 3-13: Microscope images of the crystals at different locations in 2nd vessel

3.3. Modeling results

3.3.1. Experiments to Determine Distribution Coefficients.

Distribution coefficients for C1 impurities were calculated by applying equation 1 to data obtained experimentally. A plot of the Distribution Coefficient as a function of the purity of the initial solution is shown in Figure 3-14. This information was then used to model the continuous crystallization process and determine the effect of process conditions on purity and yield. A plot of the Distribution Coefficient as a function of the purity of the initial solution is shown in Figure

3-14. This information was then used to model the continuous crystallization process and determine the effect of process conditions on purity and yield.

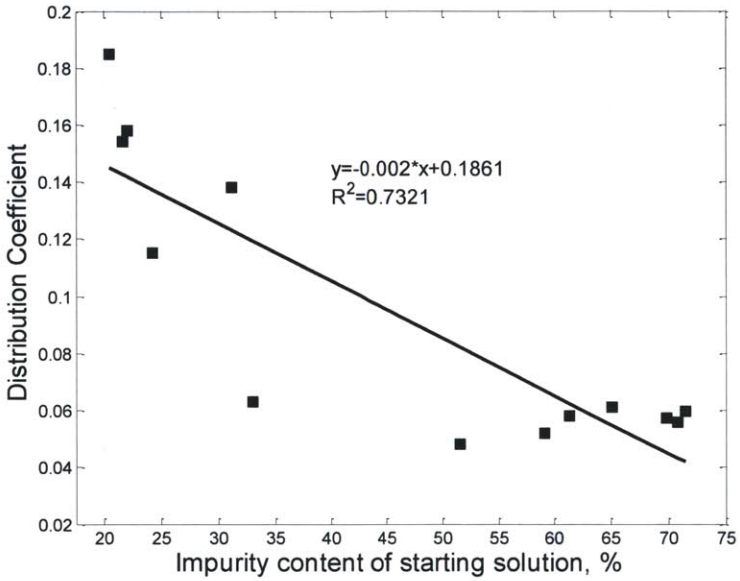

Figure 3-14: Distribution Coefficients as a function of purity of the starting solution

The variation of the distribution coefficient can be attributed to a couple of reasons. Firstly, the current crystallization process is a combined cooling-anti-solvent process. In Figure 3-14, the distribution coefficient incorporates the cooling and anti-solvent process, and there is a big variation for the distribution coefficient over the impurity level between the two procedures. And it is the main reason for the variation of the distribution coefficient in Figure 3-14. Secondly, during the experimental process, we gave same reaction time for each step to achieve equilibrium. However, there are still some deviation between the experimental state and the equilibrium state. So, it is possible that some points in Figure 3-14 showed a big deviation. Finally, the different mixing profiles and working volume can be considered to generate the experimental errors.

3.3.2. Mathematical model of cascaded multistage crystallization system.

As described in Chapter 2.7, the MSMPR model can be used to estimate the nucleation and crystal growth rate kinetic parameters by solving the optimization problem defined in equation 17. This approach was used to obtain kinetics from the continuous crystallization experiment of C1 in EtOAc-heptane. Process parameters for the experiments can be seen in Table 3-1.

Table 3-2 shows the volume based mean crystal size obtained in stages 1 and 2 as well as the supersaturation in each stage. It was observed that the mean size of C1 crystals in the each stage was not significantly different. This is because the anti-solvent was introduced in the second stage, and thus the supersaturation was kept at similar level in both stages. At the same time, a high supersaturation level in stage one was avoided and the nucleation rate and the crystal growth rate in both of the two stages were kept at the suitable level in the entire process, and the final product with higher crystallinity and better crystal morphology were generated (see Figure 3-6 & 3-7).

Table 3-1: Process conditions for estimation of nucleation and crystal growth kinetics

Condition	Value	Units
Volume Stage 1, $V1$	30	mL
Volume Stage 2, $V2$	41	mL
Flowrate Stage 1, $Q1$	0.125	mL/min
Flowrate Stage 2, $Q2$	0.174	mL/min
Temperature Stage 1, $T1$	-5	°C
Temperature Stage 2, $T2$	-10	°C
Solubility at $T1$	0.0318	Kg/Kg
Solubility at $T2$	0.0089	Kg/Kg
Concentration of API, C_o	95.2	Kg/m^3
Density of Crystal	1200	Kg/m^3
Density of Solvent	897	Kg/m^3
Density of Anti-solvent	684	Kg/m^3

Table 3-2: Mean crystal size (volume based) in stage 1 and 2

Stage	Temperature(°C)	Residence time (min)	Supersaturation	Mean Size (μm)
1	-5	240	0.35	71.69
2	-10	240	0.29	71.77

The results from the two stages were included in the optimization, and the difference between calculated and experimental crystal size distribution was minimized. To obtain an efficient optimization and accelerate convergence, the parameters k_{g0}, k_{g1}, and kb were scaled nonlinearly, using $\ln(k_{g0})$, $\ln(k_{g1})$, and $\ln(k_b)$ respectively. The results of the parameter estimation are shown in Table 3-3. A comparison between the calculated and experimental chord length distributions can be seen in Figure 3-15.

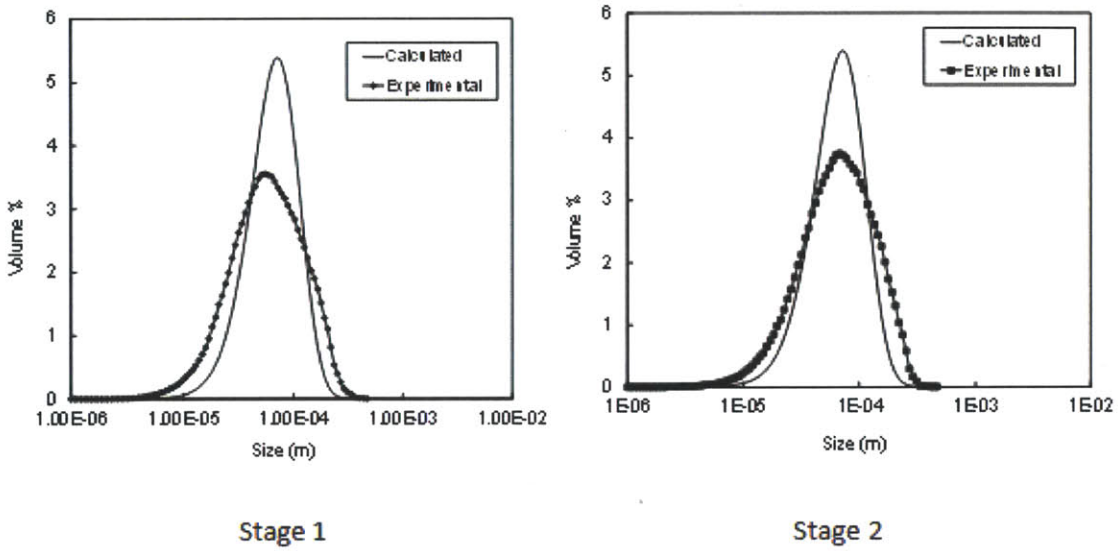

Figure 3-15: Predicted and experimental CLD for C1 continuous crystallization

Table 3-3: Estimated nucleation and crystal growth kinetic parameters

Parameter	Value	Units
k_g @ -5 °C	2.33×10^{-7}	m/min
k_g @ -10 °C	9.86×10^{-8}	m/min
k_{g0}	9.81×10^{12}	m/min
k_{g1}	12116	J/mol
k_b	6.92×10^{11}	$\#/m^3 \cdot min$
g	1.09	Dimensionless
b	3.99	Dimensionless

In order to test the validity of the model, the experiments were re-run with different parameters. The previously calculated parameters were then used to simulate the effects of changing these experimental parameters, and the results were then compared. The temperature of the first stage was changed to 0°C, and samples were taken in the two stages at steady state to measure the CLD by FBRM. As shown in Figure 3-16, the model results agree reasonably with the experimental size distribution. Linear kinetic order for crystal growth and quadratic kinetic order for nucleation are both physically realistic results. The differences between the model and the experimental data can be explained in part by the fact that C1 crystals have a needle-like morphology (Figure 3-7). One assumption of the model is that the crystals have perfectly spherical morphology, and this difference is known to impact on the accuracy of the model [57, 58, 74]. With a needle like morphology the needle width has a greater probability than the needle length of being measured by the scanning laser. For the FBRM chord length distributions, an increase in number of small chord lengths does not necessarily imply secondary nucleation, but can also be indicative of crystal growth. An increase in needle length will lead to an increase in small chord lengths counted over time.

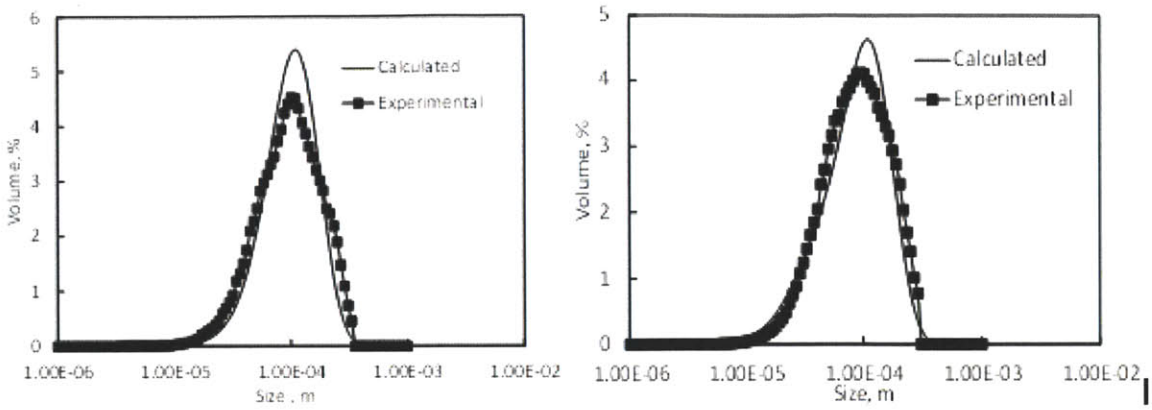

First Stage **Second stage**

Figure 3-16: Predicted and experimental CLD for C1 continuous crystallization for model validation

In addition to the spherical crystal assumption, there are a number of other assumptions involved in the population balance equation which will give rise to differences between the experimental and predicted crystal size distributions. It is assumed that the product CLD is the same as that found within the crystallizer, i.e. there is no classification of the particles in the crystallizer takes place. This is the standard assumption used in reaction engineering to define a well-mixed reaction vessel. This might not be the case if there is imperfect mixing or dead zones in the vessel. Secondly, it is assumed that particles are formed only by nucleation and increase in size only through growth and that the processes of breakage, attrition, and agglomeration are negligible. In the real system, agglomeration and the breakage of the crystals are inevitable and can be a significant factor especially for systems with needle morphology. Finally, because the crystals are needles, the assumption that shape factors for particles are not a function of size may not be completely accurate. Unlike spheres, a needle cannot be described with a single characteristic size, unless the aspect ratios for all needles are equivalent. Breakdowns in these assumptions provide additional deviations when comparing the model with the experimental data.

3.3.3. Effect of Process Conditions on Crystal Purity and Yield.

The multistage MSMPR model was used to evaluate the effect of operating conditions on the purity of the crystal and the process yield in the continuous crystallization process of C1. The influence of the temperature and residence time of both of the two stages on the crystal purity and the process yield are evaluated. The effect of the temperature of each stage on the product yield purity can be seen in Figure 3-17. For comparison, in the batch experiments at -5°C, and -10°C, the purity of the crystals was 89.60% and 88.48%, respectively.

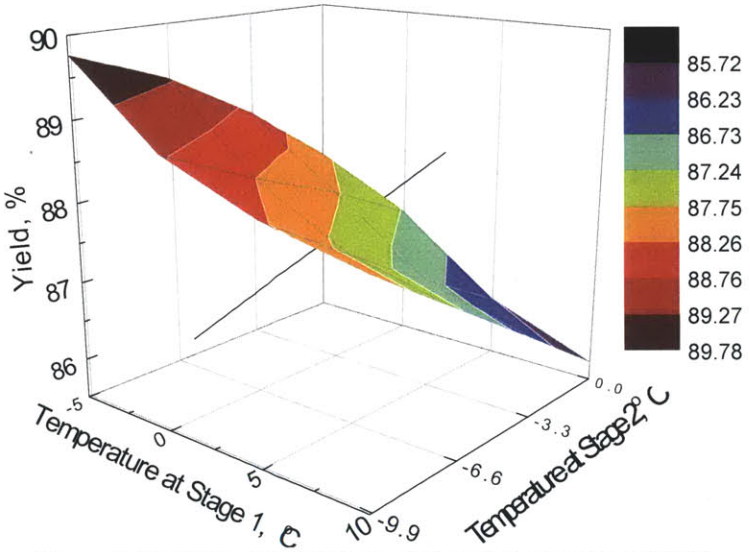

Figure 3-17: Effect of temperature of stage 1 & 2 on process yield

Changing the temperature of each stage has a significant effect on the process yield. By varying the temperature by 15°C from the actual chosen operating temperatures, the yield decreased from 89.8% to 85.7%. This is because the solubility of C1 increases with increasing temperature. Increasing the temperature even further would decrease the yield even more.

The effect of the temperature of each stage on the final crystal purity was also studied, and the results can be seen in Figure 3-18.

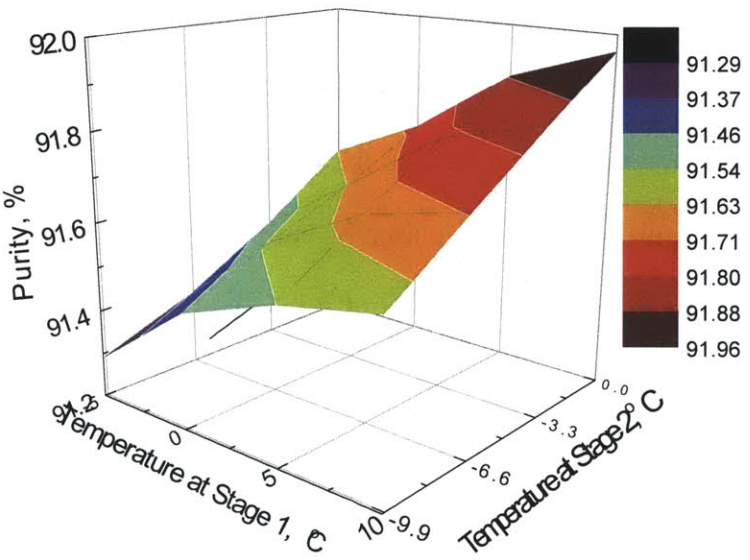

Figure 3-18: Effect of temperature of stage 1 & 2 on crystal purity

The results indicate that changing the temperatures of the stages results in a maximum purity difference of 0.7%. That is because the entire process included anti-solvent crystallization process and cooling process, and the influence of only temperature as shown here is not so significant. As the temperature in second stage increases, the purity of the crystals also increases. This is due to the fact that, at steady state, the concentration of the impurities in the liquid phase in second stage is reaching a higher level when the temperature is lower. The results from Figure 18 and Figure 19 show that the temperatures at both of the two stages have opposite effects on purity and process yield. As process yield is increased, product purity decreases.

The influence of the residence time on the yield and purity of the final product were also evaluated as well and the results are shown in Figures 3-19 and 3-20. The residence time of each stage was varied between 120-800 minutes. The product yield varied from 87.5% to 91.0%. The kinetics of crystal growth for C1 are quite slow, so it takes a very long time for the concentration to reach the solubility limit. Not surprisingly, when the second stage had a very long residence time, the residence time of the first vessel did not affect the product yield significantly. For the product purity, the crystal purity decreased with increasing residence time. Increasing the

residence time of the first vessel showed a greater effect on the purity than decreasing the residence time of the second vessel. The product purity ranged from 91.0% to 91.6%. Again, there was a negative correlation between product purity and yield when changing the residence time.

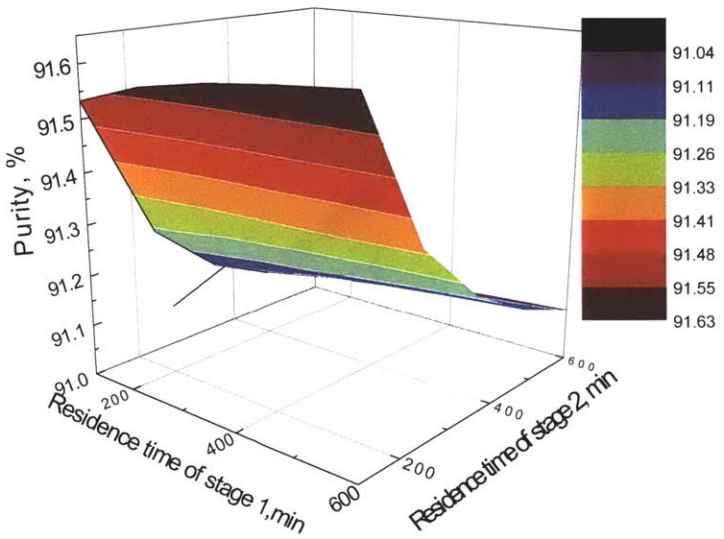

Figure 3-19: Effect of residence time of stage 1 & 2 on crystal purity

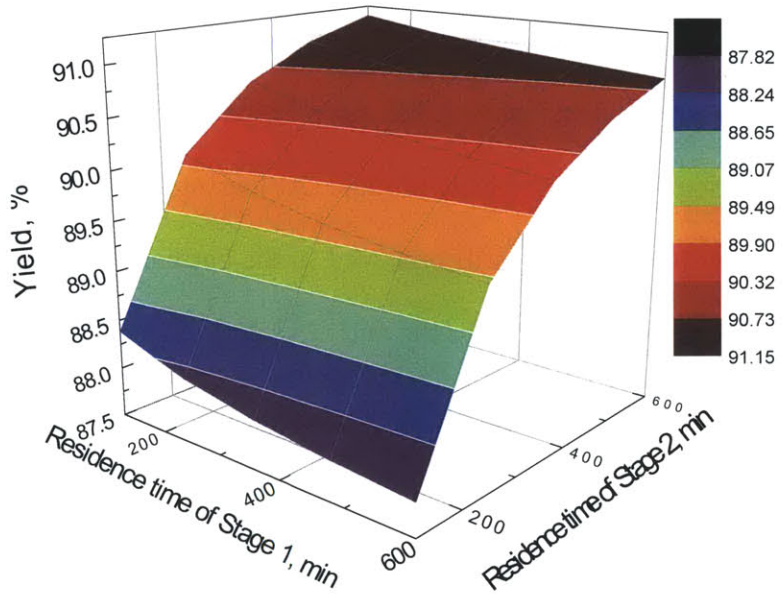

Figure 3-20: Effect of residence time of stage 1 & 2 on process yield

The relationship between the purity of the final product and the process yield has been correlated and it can be clearly seen that the opposite influence of process parameters on the

purity and yield. This behavior is shown in Figure 3-21. The model was used to evaluate the effect of process parameters on the purity of the crystals and the process yield. The results of the model could be used to find out the optimal operating conditions to maximize yield without having too high impurity content.

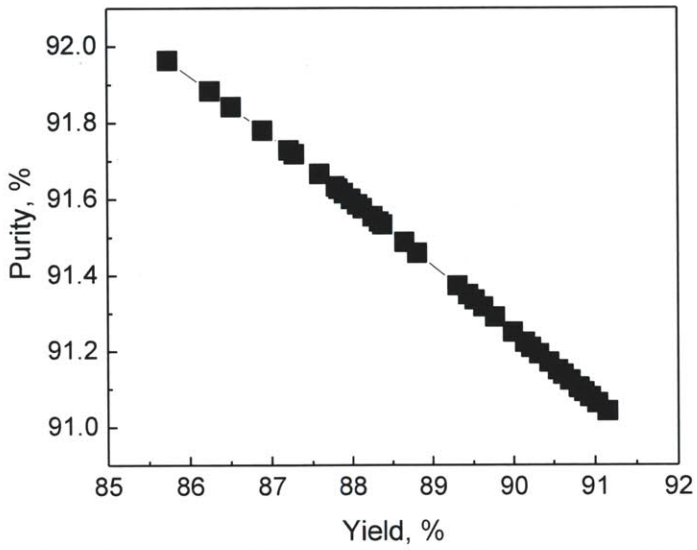

Figure 3-21: Purity of the crystals as a function of process yield

Attributed to the growing interest in the development of continuous crystallization processes in the pharmaceutical industry, it has been an urgent requirement to develop robust continuous crystallization processes which produce API crystals with high yield and purity. While batch manufacturing process is still preferred in the current pharmaceutical industry, the development of continuous systems such as the one described in this paper will help the industry in moving from batch to continuous manufacturing.

3.4. Conclusions

A multistage cascaded MSMPR continuous crystallization system was optimized for the continuous crystallization of Aliskiren boc-base using cooling and anti-solvent to generate supersaturation. Its capability to crystallize an organic compound was experimentally

demonstrated. XRPD results indicate that the vessel in which anti-solvent is added has a significant influence on the final crystal properties. Adding anti-solvent in the second vessel resulted in crystals with increased crystallinity and better morphology for downstream processing. Focused Beam Reflectance Measurement (FBRM) technology was employed to track the crystals size distribution of Aliskiren boc-base. A mathematical model was used to analyze the experimental results. By combining the process model with an optimization algorithm, the nucleation and growth rate parameters were extracted and used to predict the size distribution under different process conditions. The multistage MSMPR model was used to evaluate the effect of process conditions, including the temperature and residence time, on the purity of the crystal and the process yield in the continuous crystallization process of Aliskiren boc-base.

4. CRYSTALLIZATION OF ALISKIREN HEMIFUMARATE

4.1. Introduction

Chapter 4 describes the second of the continuous crystallization steps developed for the bench scale continuous manufacturing platform. Unlike the crystallization for Aliskiren boc-base which was an anti-solvent and cooling crystallization, the crystallization of Aliskiren hemifumarate is a simultaneous reaction and crystallization step. Due to the solubility and filtration behavior, a number of different solvent combinations and operating temperatures were iterated before the final operating conditions were found. This system was also modeled using the distribution coefficient model and the population and mass balance equations defined in Chapters 2.5 and 2.6.

4.2. Process development

Fumaric acid is nearly insoluble in ethyl acetate. Because of this, ethanol was added to solubilize the acid. Adding ethanol to the ethyl acetate stream, however, increased the solubility of Aliskiren, as can be seen in Figure 4-1. The higher final solubility results in an overall lower yield, so great care was taken to avoid adding more ethanol than necessary. Fumaric acid solubility in ethanol at 70°C is approximately 11 w/w%, so this was chosen as the starting point[75]. Because 70°C is close to the boiling point of ethanol, in order to avoid evaporating too much of the solvent, the ethanol was diluted with an equal mass of ethyl acetate. Experiments showed that the solubility of fumaric acid on a per mass of ethanol basis increased slightly after adding ethyl acetate, so there were no concerns about the fumaric acid precipitating out. Preventing the evaporation of the ethanol was also important because the ratio of fumaric acid to Aliskiren freebase is paramount to the success of the crystallization. If the ratio is too low, then

the resulting product would be a mixture of the freebase and the hemifumarate form. If the ratio is too high, then the yield of the process is significantly decreased, with ratios of 0.75 or greater resulting in nearly no crystals. This is likely due to the formation of a fumarate salt in solution, though this was not experimentally determined.

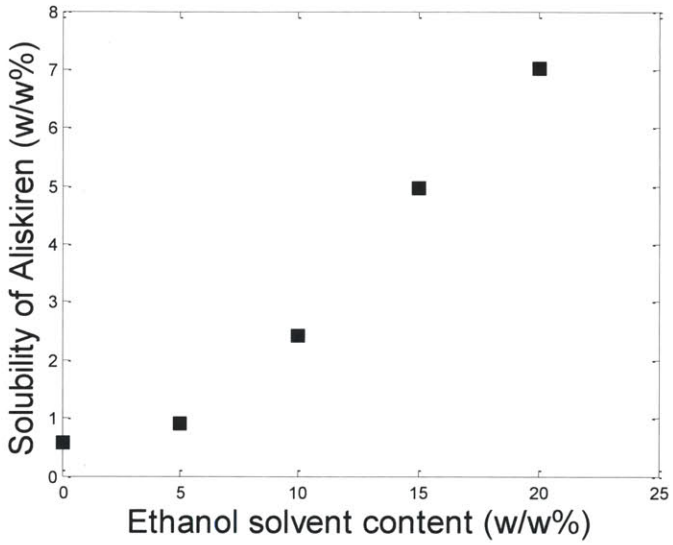

Figure 4-1: Solubility of C3 as a function of ethanol solvent content

The next design step was to choose the temperatures of the two stages. The solubility of Aliskiren Hemifumarate as a function of temperature can be seen in Figure 4-2. As expected, the lower the temperature, the lower the solubility. To maximize yield, the temperature of the two stages should be as low as possible, but there were other circumstances to consider. Because the reaction takes place in solution in the first stage, it was decided that the temperature of that stage should be higher to avoid overly rapid supersaturation generation. In addition, if the temperature was too low, the fumaric acid could precipitate faster than it reacted with the free base, which would prevent the formation reaction of the hemifumarate. Thus, an operating temperature of 20°C was chosen. For the second vessel, to maximize the yield of the process, an operating temperature of -10°C was chosen. This temperature was low enough to maximize yield without

going beyond the capacity of the refrigerated circulators and without decreasing the growth rate of the crystals too much.

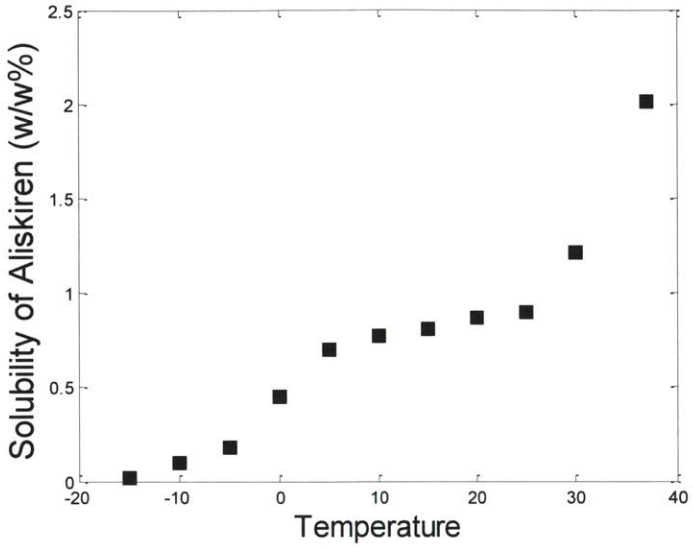

Figure 4-2: Solubility of C3 at 95/5 (w/w%) ethyl acetate/ethanol solvent composition

4.3. Technical Challenges and crystallization results

The operation of this crystallization had some significant technical difficulties. Because of the scale of the crystallizations, the slurry flow rates between the vessels were very low. Had the pumps been set to pump continuously, the flow rate would have been 0.17 mL/min. To achieve that flow rate, the tubing between the vessels would have to be very small, and this would cause issues with clogging. In addition, the low flow rate would cause issues with settling of the solids in the pump lines. In order to mitigate this issue, the pumps were turned on at set intervals of time at very high flow rates. In this way, the slurry was moved very quickly between vessels, avoiding issues with settling. Also, wider tubing was used to avoid issues with clogging of the lines. The pumps were set to operate once every 20 minutes, such that less than 10% of the contents of each stage were transferred in each step. Another technical issue involved the pumping of the fumaric acid. Because the concentration of the fumaric acid in the solution was close to saturation at 70°C, as the solution was transferred to the first stage of the crystallization,

the line would often become clogged. This was primarily because the fumaric acid solution decreased in temperature inside of the tubing and thus the fumaric acid precipitated uncontrollably. To solve this problem, the transfer lines were changed to metal tubing, with only a small section of plastic tubing inside of the peristaltic pump head. In addition, the metal tubing was covered with heating tape heated to 70°C in order to maintain the temperature.

The continuous crystallization system was run for 48 hours, with samples taken intermittently to check for steady state. In typical experiments, the concentration of the mother liquor after the first stage was approximately 1 w/w% Aliskiren. After the second stage, the mother liquor concentration was approximately 0.5%. Both of these values are very close to the equilibrium values, and matched closely with batch experiments. At typical loadings of 6.5%, these mother liquor concentrations would result in yields of 85% and 92.3% in the first and second stages, respectively. Recycles could be used to increase this yield if it was deemed too low. After filtration, the mother liquor could be concentrated by evaporating some of the solvent, and this concentrated stream could be sent back to one of the stages for further crystallization. Investigations of recycle streams are beyond the scope of this work.

An optical microscope picture of Aliskiren Hemifumarate crystals produced using the previously described continuous crystallization method can be seen in Figure 5. The crystals have needle-like morphology with a length of around 50 micrometers. Crystals produced in batch using the same solvent composition and final operating conditions (stirring rate, temperature etc.) were of a similar size. Thus, the continuous crystallization produced crystals with very similar physical properties. In Figure 4-3, an XRPD pattern of the final crystallized product can be seen. The crystals exhibit some sharp peaks, but lack a strong baseline, indicating some amorphous content.

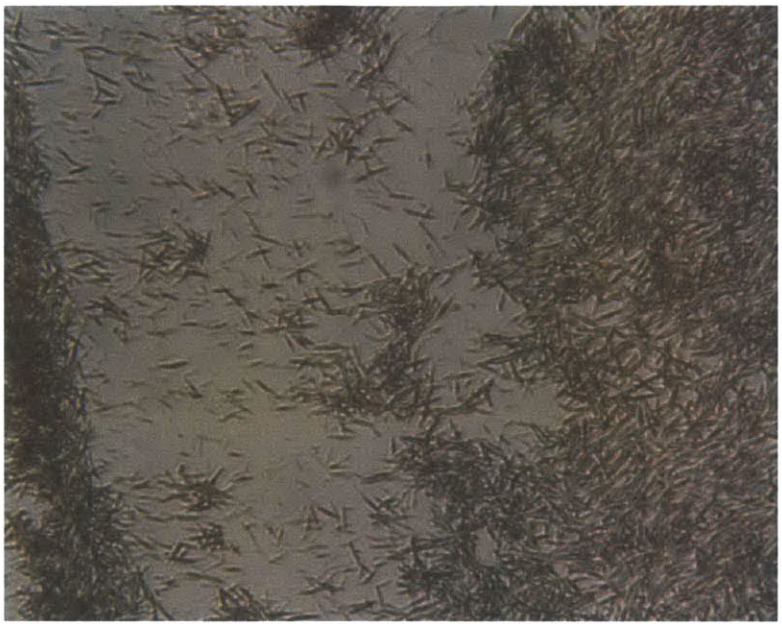

Figure 4-3: Optical Microscope picture of crystallized Aliskiren Hemifumarate

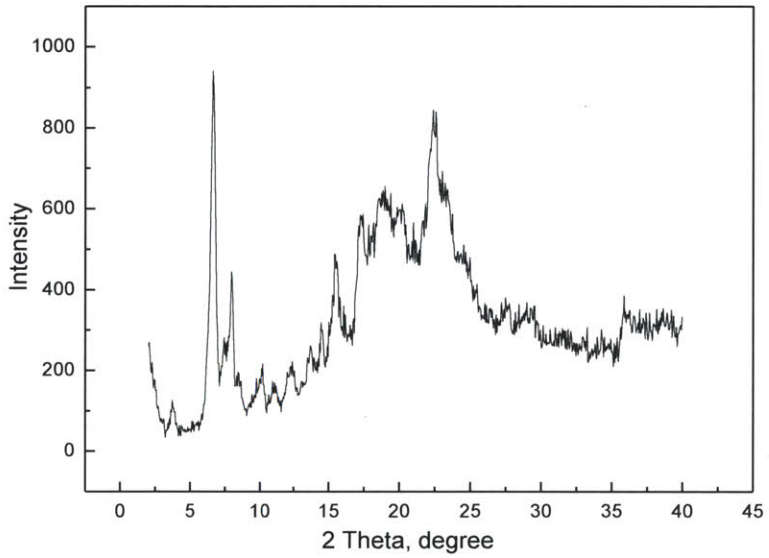

Figure 4-4: XRD pattern of crystallized product

4.4. Modeling results

4.4.1. Experiments to determine equilibrium Distribution Coefficients

Distribution coefficients for C3 impurities were calculated by applying equation 1 to data obtained experimentally. A plot of the Distribution Coefficient as a function of the purity of the

initial solution is shown in Figure 4-5. This information was then used to model the continuous crystallization process and determine the effect of process conditions on purity and yield.

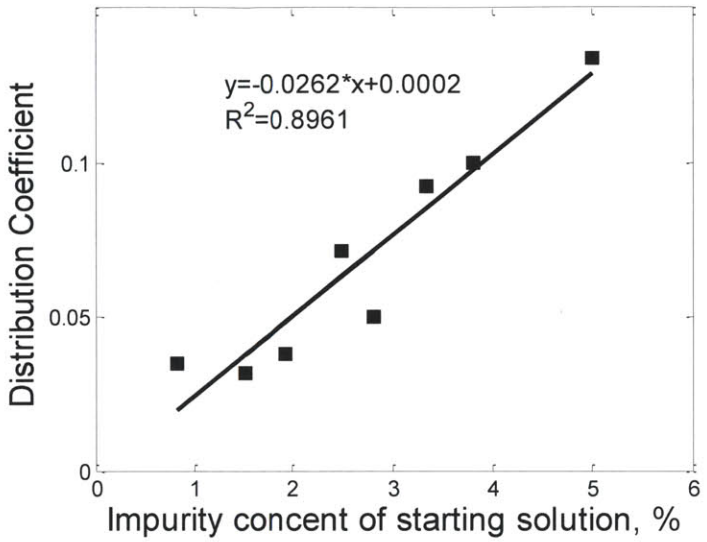

Figure 4-5: Distribution coefficients for Aliskiren Hemifumarate

4.4.2. Mathematical Modeling and Parameter Fitting

As described in the previous section, the MSMPR model can be used to estimate the nucleation and crystal growth rate kinetic parameters by solving the optimization problem defined in equation 17. This approach was used to obtain kinetics from continuous crystallization experiments of Aliskiren in EtOAc-EtOH. Process parameters for the experiments can be seen in Table 4-1.

Table 4-1: Process conditions for estimation of nucleation and growth parameters

Condition	Value	Units
Volume Stage 1, V_1	30	mL
Volume Stage 2, V_2	30	mL
Total Flowrate, Q	0.125	mL/min
Temperature Stage 1, T_1	25	°C
Temperature Stage 2, T_2	-10	°C
Solubility at T_1	0.009	Kg/Kg
Solubility at T_2	0.001	Kg/Kg
Concentration of API, C_o	63.9	Kg/m^3
Density of Crystal	1200	Kg/m^3
Density of Solvent	891.6	Kg/m^3

The model is built based on the population balance, which is based on the concept of continuous mixed-suspension, mixed product-removal (MSMPR) crystallizers developed by Randolph and Larson (1971) and its power of the population balance for analysis of crystallizers is demonstrated by its application to a continuous crystallizer [17, 18, 21]. The results from the two stages were included in the optimization, and the difference between calculated and experimental crystal size distribution was minimized. To obtain an efficient optimization and accelerate convergence, the parameters k_{g0}, k_{g1}, and k_b were scaled nonlinearly, using $\ln(k_{g0})$, $\ln(k_{g1})$, and $\ln(k_b)$ respectively. The results of the parameter estimation are shown in Table 4-2, and a comparison between the calculated and experimental crystal size distributions can be seen in Figure 4-6.

Table 4-2: Estimated nucleation and growth parameters

Parameter	Value	Units
k_g @ 25°C	1.55×10^{-8}	m/min
k_g @ -10°C	4.17×10^{-9}	m/min
k_{g0}	0.00029	m/min
k_{g1}	2935	J/mol
k_b	3.2×10^{7}	#/m^3 min
g	1.08	Dimensionless
b	1.95	Dimensionless

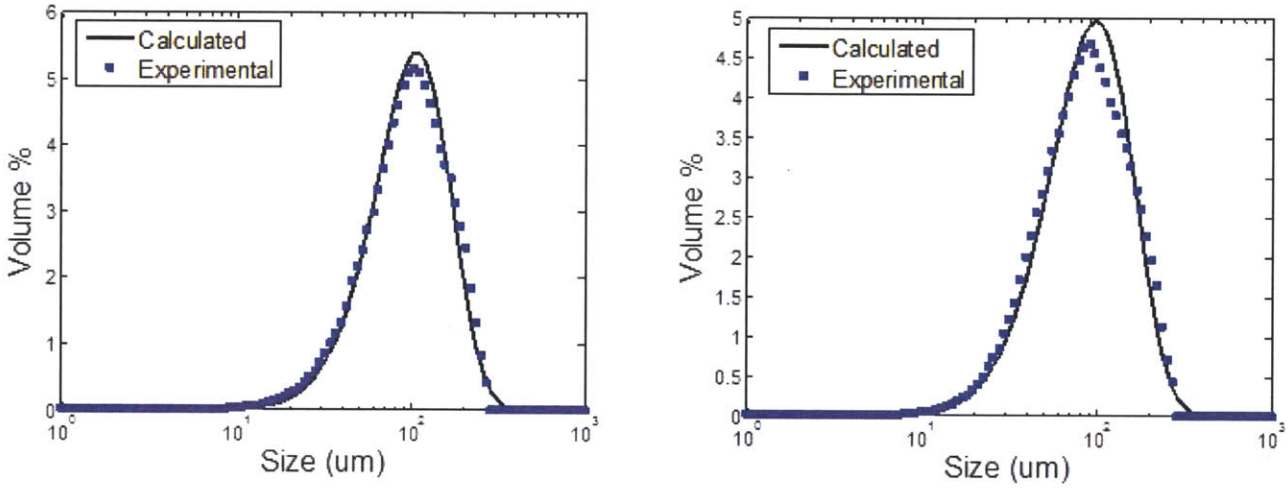

Figure 4-6: Fitted chord length distributions for vessels 1 (left) and 2 (right)

FBRM was employed to obtain the experimental crystal size distribution. As shown in Figure 4-6, the model results agree very well with the experimental size distribution. The small differences between the model and the experimental data can be explained in part by the fact that Aliskiren crystals have a needle-like morphology (Figure 5). One assumption of the model is that the crystals have perfectly spherical morphology, and this difference is known to impact on the accuracy of the model [8, 57]. Because the crystals were assumed to be spheres, a single characteristic size was used as a measure of the size of the particles [74]. With a needle like morphology the needle width has a greater probability than the needle length of being measured by the scanning laser. For the FBRM chord length distributions, an increase in number of small

chord lengths does not necessarily imply secondary nucleation, but can also be indicative of crystal growth. An increase in needle length will lead to an increase in small chord lengths counted over time.

In addition to the spherical crystal assumption, there are a number of other assumptions involved in the population balance equation which will give rise to differences between the experimental and predicted crystal size distributions. It is assumed that the product CLD is the same as that found within the crystallizer, neglecting classification of the particles in the crystallizer. This is the standard assumption used in reaction engineering to define a well-mixed reaction vessel. This might not be the case if there is imperfect mixing or dead zones in the vessel. Secondly, it is assumed that particles are formed only by nucleation and increase in size only through growth and that the processes of breakage, attrition, and agglomeration are negligible. In the real system, agglomeration and the breakage of the crystals are inevitable and can be a significant factor especially for systems with needle morphology. Finally, because the crystals are needles, the assumption that shape factors for particles are not a function of size may not be completely accurate. Unlike spheres, a needle cannot be described with a single characteristic size, unless the aspect ratios for all needles are equivalent. Breakdowns in these assumptions provide additional deviations when comparing the model with the experimental data.

4.4.3. Effect of Process Conditions on Crystal Purity and Yield.

The multistage MSMPR model was used to evaluate the effect of operating conditions on the purity of the crystal and the process yield in the continuous crystallization process of Aliskiren Hemifumarate. The influence of the temperature and residence time of both of the two stages on the crystal purity and the process yield are evaluated. The effect of the temperature of each stage on the product purity can be seen in Figure 4-7.

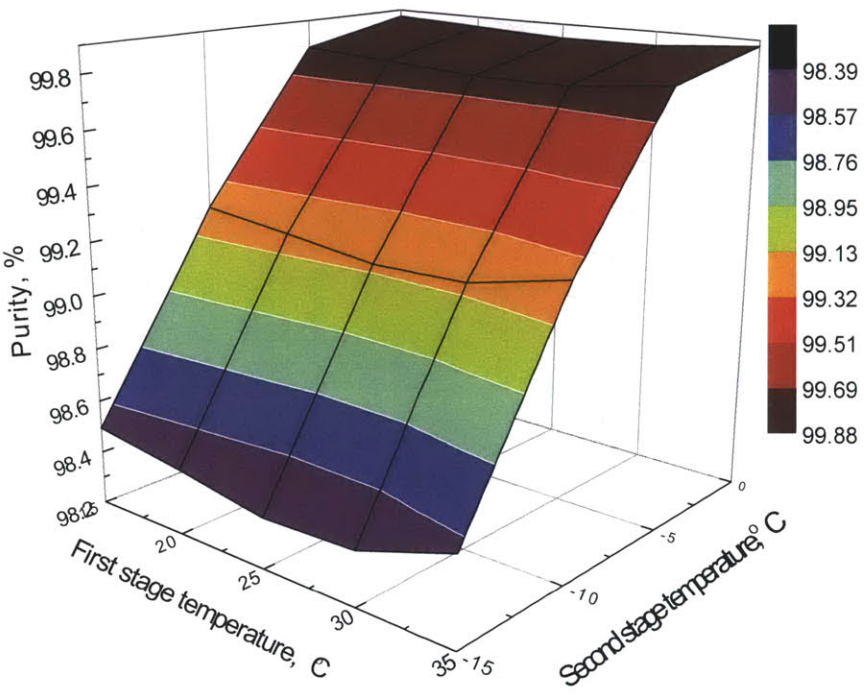

Figure 4-7: Effect of temperature of stage 1 and 2 on crystal purity

Changing the temperature of each stage has a moderate effect on the crystal purity. By varying the temperature of each stage by 15 degrees from the actual selected operating temperatures, the purity decreased from 99.8% down to 98.4%. This is because the solubility of Aliskiren Hemifumarate increases with increasing temperature. Increasing the temperature even further would decrease the yield even more.

The effect of the temperature of each stage on the final process yield was also studied, and the results can be seen in Figure 4-8.

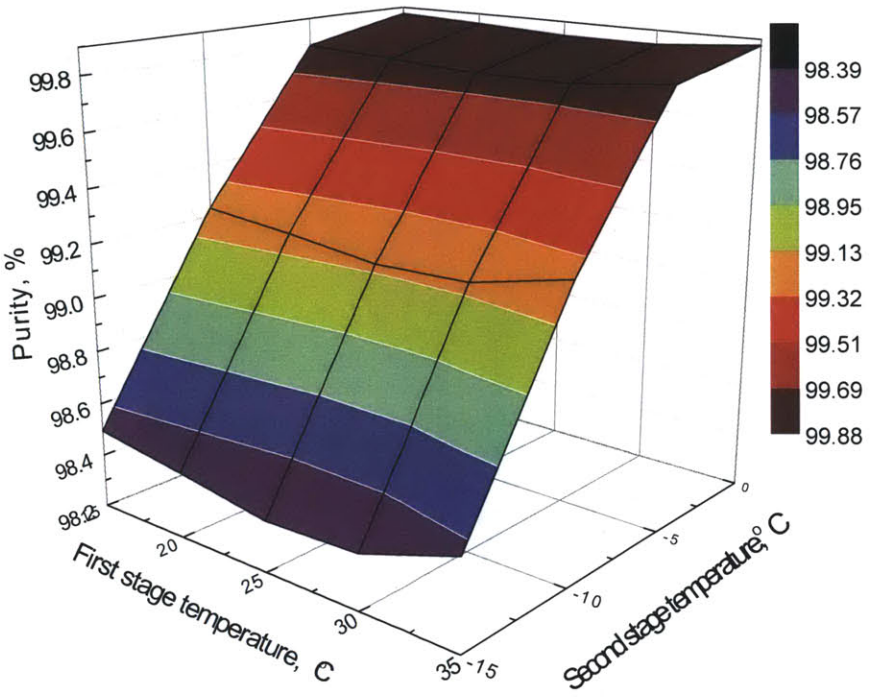

Figure 4-8: Effect of temperature of stage 1 and 2 on process yield

The results indicate that changing the temperature of the stages has a great influence on the process yield. Changing the temperature of each stage by 15°C resulted in a yield range from 90% down to nearly 40%. Even though the crystallization is a reactive crystallization, the final salt is still fairly soluble in the solvent system at moderate temperatures. The results from Figure 9 and Figure 10 show that the temperatures at both of the two stages have opposite effects on purity and process yield. As process yield is increased, product purity decreases.

The influence of the residence time on the yield and purity of the final product were also evaluated as well and the results are shown in Figures 4-9 and 4-10. The residence time of each stage was varied between 120 and 600 minutes. The final crystal purity varied from 97.6% at the longest residence times to 99.6% at the shortest residence times.

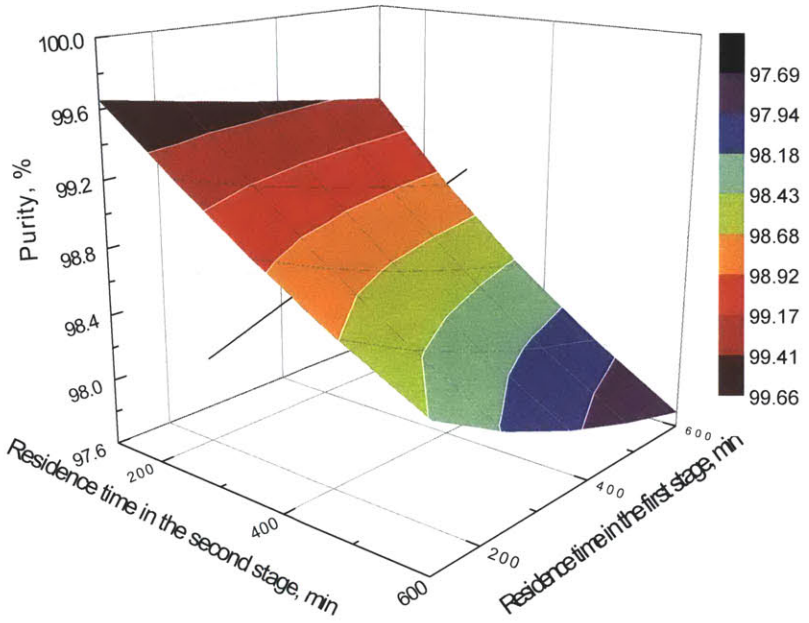

Figure 4-9: Effect of residence time of stages 1 and 2 on crystal purity

The product yield ranged from 71% at the shortest residence times to 93.6% at the longest residence times. Increasing the residence time of the first vessel increased the product yield more significantly than changing the residence time of the second vessel. At a residence time of 120 min in vessel 1 and 600 min in vessel 2, the yield was only 81.2%, but with a residence time of 600 min in in vessel 1 and 120 min in vessel 2, the yield was 90.8%. Because Aliskiren Hemifumarate is a slow growing molecule, the effects of having a higher temperature on the growth rate are magnified. Because vessel 1 was operated at a much higher temperature, it is logical that the increased temperature and residence time in vessel one would result in a higher final yield than the same residence time in the much colder second vessel. Again, there was a negative correlation between product purity and yield when changing the residence time.

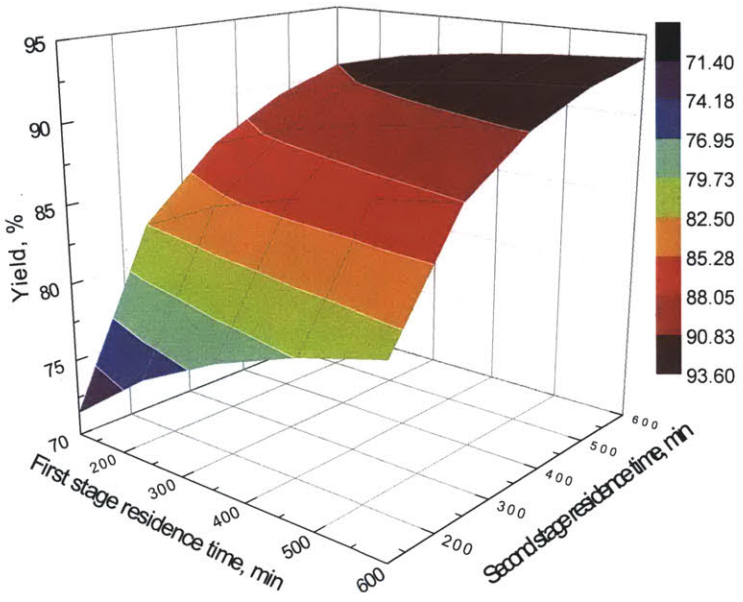

Figure 4-10: Effect of residence time of stages 1 and 2 on process yield

The relationship between the purity of the final product and the process yield has been correlated and it can be clearly seen that the opposite influence of process parameters on the purity and yield. This behavior is shown in Figure 4-11. The results of the model could be used to find out the optimal operating conditions to maximize yield without having too high impurity content.

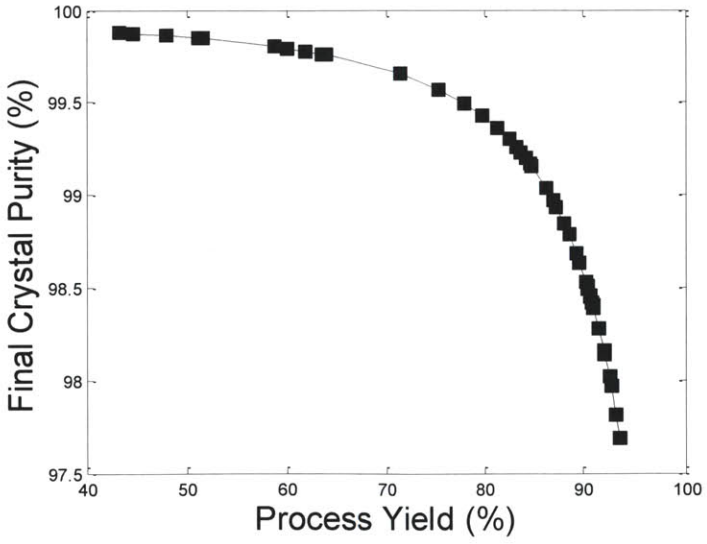

Figure 4-11: Purity of crystals as a function of process yield

4.5. Conclusions

A multistage cascaded MSMPR continuous crystallization system was optimized for the continuous reactive crystallization of Aliskiren Hemifumarate using cooling to generate supersaturation. The process to produce crystals at both high yield (>92%) and purity (99%). with good crystal morphology was demonstrated. Though increasing the process yield results in a less pure crystal, even at 94% yield, the A number of technical challenges rising from working at such a small scale were solved. Focus Beam Reflectance Measurement (FBRM) technology was employed to track the crystals size distribution of Aliskiren Hemifumarate crystals. A mathematical model was used to analyze the experimental results. By combining the process model with an optimization algorithm, the nucleation and growth rate parameters were extracted. The multistage MSMPR model was then used to evaluate the effect of process conditions – temperature and residence time – on the purity of the final crystals and the process yield. The results showed that the crystal purity and process yield had a monotonic relationship, wherein as one increased, the other decreased. This crystallization process is now ready to integrate into the end-to-end continuous manufacturing demonstration unit.

5. TEMPLATED NUCLEATION ON SPHERICAL AGGLOMERATES

5.1. Introduction

Chapter 5 is the first of two chapters to describe new experimental techniques using spherical agglomerates made through evaporative water-in-oil crystallization. In this chapter, induction time measurements for the crystallization of acetaminophen in the presence of single crystal and spherical lactose and mannitol are shown. The significant difference in induction time between the single crystal and lactose cases will be explained through the significant differences in crystal morphology. An in-depth look at the epitaxy between the acetaminophen and the lactose will reveal coincident lattice matches between the fastest growing faces of acetaminophen and one of the new faces of lactose that is present in the spherical agglomerate that is not present in the single crystal lactose. Additionally, molecular dynamics simulations further show that the interactions between the new faces of lactose and the fastest growing faces of acetaminophen are highly energetically favorable.

5.2. Generation of Spherical Agglomerates

Spherical agglomerates of triclinic lactose and the β polymorph of D-mannitol were generated using the method outlined in the experimental section. Optical micrographs and SEM images of spherical agglomerates of lactose crystals can be seen in Figure 5-1. The agglomerates were filtered after crystallization and analyzed using SEM. The agglomerates were composed of many single crystals. The individual crystals making up the agglomerates were small (<1 microns). The crystal form of lactose comprising the spherical agglomerates was found to be the triclinic polymorph.

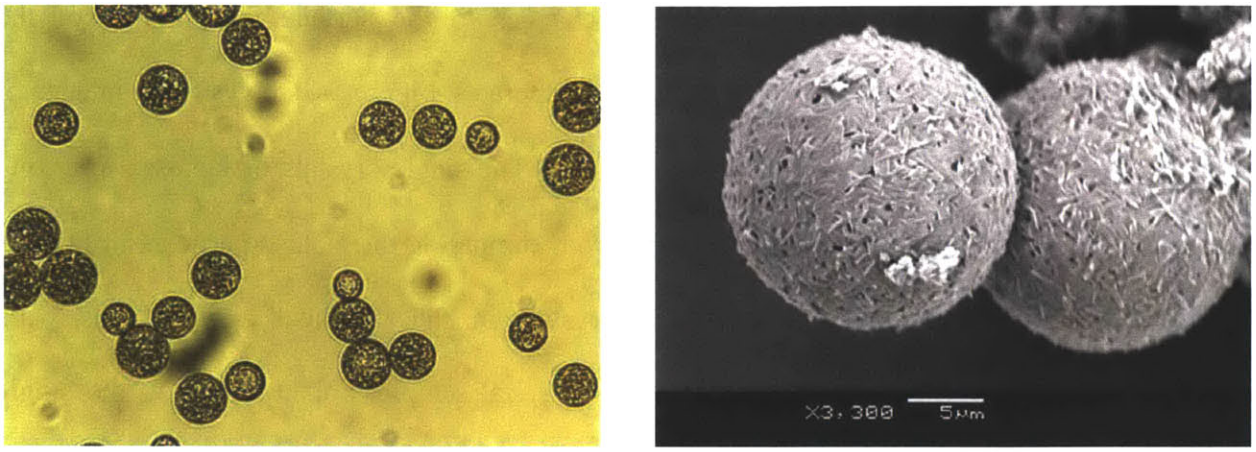

Figure 5-1: Optical microscopy image (left) and SEM image (right) of Triclinic Lactose Spherical Agglomerates. Individual crystals comprising the spherical agglomerates are on the nanometer scale in length

Figure 5-2 shows optical micrographs and SEM images of spherical D-mannitol agglomerates. The optical micrograph shows there is little bulk nucleation, and that the mannitol crystallized as spherical agglomerates with diameters between 5 – 30 µm. This can be seen in greater detail in the SEM image. The β polymorph crystallized, as will be shown in XRPD data to be discussed later. The individual crystals comprising the spherical agglomerates were very small, some on the scale of hundreds of nanometres.

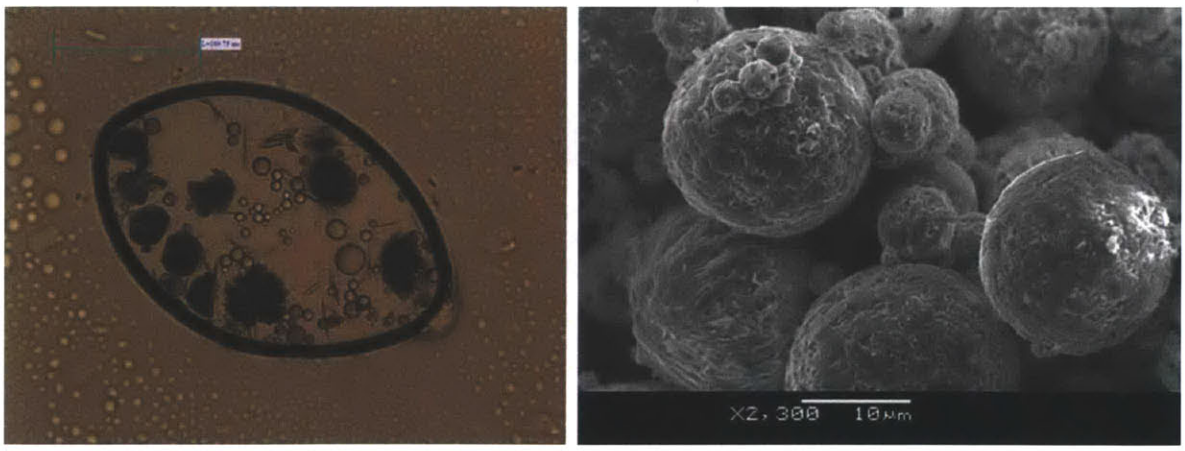

Figure 5-2: Optical microscope image (left) and SEM image (right) of β-Mannitol Spherical Agglomerates. Crystals comprising the spherical agglomerates are on the order of nanometers in length.

Image analysis was used to determine changes to the surface morphology of the substrates due to crystallizing them as spherical agglomerates. Figure 5-3 shows SEM images of single crystals of triclinic lactose and (β)-D-mannitol. The single crystals of lactose were long thin plates between 5 and 30 microns in length. From comparing the lactose particles in Figures 5-1 and 5-3, it is evident that the lactose crystals in the spherical agglomerates were morphologically different from those in the single crystal sample. For D-mannitol, the single crystals in Figure 5-3 range from 20 microns to 200 microns in length (for the long axis), much larger than the diameter of the spherical agglomerates. The morphology of the mannitol crystals in each image is different. Each system was analyzed using XRPD to study the morphological differences in more detail.

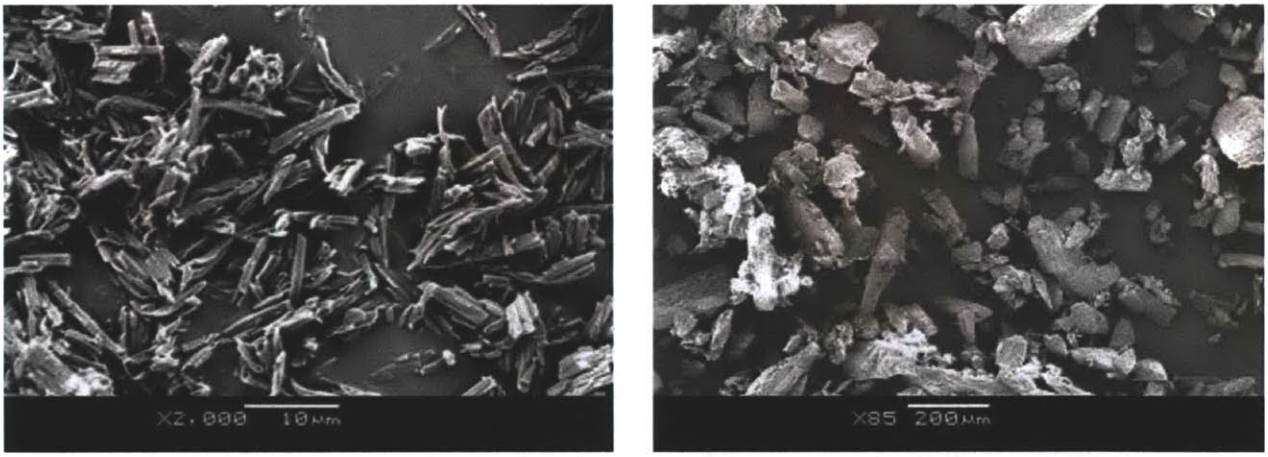

Figure 5-3: SEM image of single crystals of triclinic lactose (left) and beta mannitol (right). Morphology of the lactose is significantly different than that of the single crystals comprising the spherical agglomerates. Single crystals of mannitol are often large

X-ray powder diffraction characterization

XRPD measurements of the single crystal and spherical forms of each substrate were taken. Figure 5-4 shows the measured powder patterns for single crystal mannitol, spherically agglomerated mannitol, and the calculated powder pattern for the β polymorph (REF code

DMANTL07) of mannitol. The single crystal and agglomerated D-mannitol are the β polymorph. The agglomerated D-mannitol had nearly identical diffraction peaks in terms of location and intensity as the single crystals, even though the morphology of the D-mannitol crystals changed significantly. There was one unique peak at 9.7°, which was not present in either the XRPD data of single crystal D-mannitol or the calculated pattern for the β polymorph. This peak does not correspond to any other known polymorphs of D-mannitol. It is possible this is due to an undiscovered polymorph, but more likely due to an amount of solid impurity.

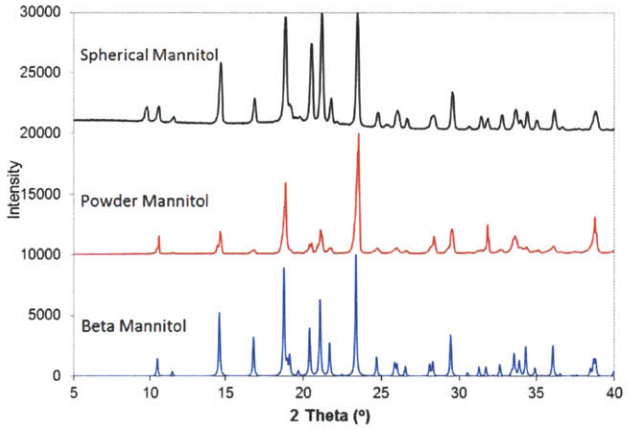

Figure 5-4: XRPD data for Mannitol. The diffraction patterns for the spherical and powder D-mannitol are nearly identical and match up almost perfectly with the calculated powder pattern for beta mannitol

X-ray powder diffraction data for lactose are shown in Figure 5-5. Single crystal and agglomerated lactose data are shown along with the calculated powder pattern for triclinic lactose (REF code EYOCUQ01) for comparison. Though both the single crystal and agglomerated lactose are the triclinic polymorph, the diffraction patterns have important differences. Peaks were present in the spherical agglomerate powder pattern that did not correspond to peaks in the measured pattern of powder triclinic lactose, but were found in the calculated powder pattern of triclinic lactose. The miller indices of the faces represented by these peaks were assigned by finding the equivalent peaks in the calculated powder pattern. The four

most intense new peaks were identified as the $(0\bar{3}1)$, $(20\bar{1})$, (140), and $(14\bar{1})$ crystal planes. Unlike for D-mannitol, the change of morphology in the lactose crystals comprising the spherical agglomerates led to the formation of new crystal faces. For the new peaks of lactose we were not able to explicitly ascribe any of them as originating from the surface of the agglomerates. However, the experimental and computational analysis described below is indicative that the $(14\bar{1})$ plane is exposed on the surface.

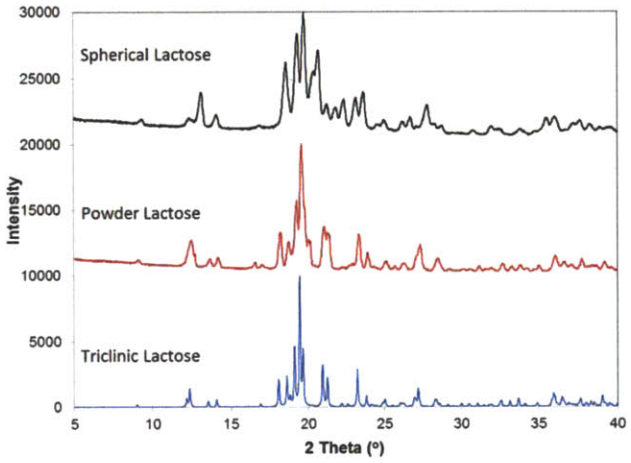

Figure 5-5: XRPD data for Lactose. Diffraction patterns for the spherical and powder lactose have some significant differences. Additional peaks in spherical lactose correspond to peaks in the triclinic lactose calculated powder pattern

5.3. Nucleation Induction Time

The effect of the modified substrate morphology on the nucleation induction time for AAP from ethanol at a σ of 1.36 was studied following the X-ray analysis. The induction time τ was measured without using a substrate and using both single crystal and spherically agglomerated triclinic lactose and D-Mannitol. We hypothesized the presence of different crystal faces in the spherical agglomerates of lactose may change the nucleation kinetics of Form I AAP through a change in the heterogeneous nucleation mechanism. Because no change in the available crystal faces of D-mannitol was observed for the spherical agglomerates, we predicted

that no statistically significant change in nucleation kinetics would be observed. τ was calculated using the following statistical analysis. It was assumed that the nucleation induction time followed a Poisson distribution [33, 76-78]. If λ represents the number of expected occurrences of some event in a time interval, then the probability of k occurrences is

$$f(\lambda, k) = \frac{\lambda^k e^{-\lambda}}{k!} \quad (1)$$

By setting $k = 0$ and $\lambda = t / \tau$, then the probability that no nucleation event will occur (P) within a given time t is given by:

$$P = exp\left(\frac{-t}{\tau}\right) \quad (2)$$

$$ln(P) = \frac{-t}{\tau} \quad (3)$$

Figure 5-6 is a plot of $ln(P)$ versus t, i.e. the probability that a crystallization event has not occurred after t minutes. Linear regression was performed on the data plotted in Figure 5-6 such that the induction time (τ) and associated error could be determined from equation (3).

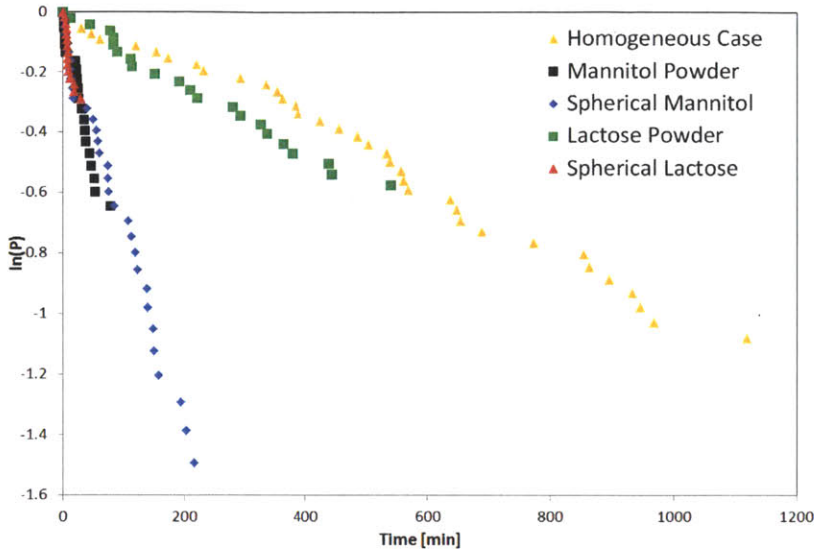

Figure 5-6: Plot of the log of the probability that an AAP crystallization event would not occur plotted versus time. Crystallizations of AAP in presence of spherical lactose show significantly faster kinetics than crystallizations in presence of powder lactose, while crystallizations in presence of spherical and powder mannitol show similar kinetics

The values of τ for each experiment are presented in Table 5-1. AAP nucleation from the bulk resulted in τ = 1020 minutes. τ in the presence of single crystal D-mannitol was ~ 130 minutes, and for the spherical agglomerates ~ 140 minutes, nearly identical within experimental and calculated error. For lactose, nucleation induction time of Form I AAP in the presence of spherical agglomerates showed a greater decrease in τ compared to that when using single crystals. The induction time decreased from 840 minutes for single crystals of lactose to 73 minutes for the spherical agglomerates.

Table 5-1: Nucleation induction time (in minutes) for AAP crystallizations. Induction time for spherical triclinic lactose is 11x faster than for powder lactose. Induction times for powder and spherical mannitol are approximately the same

Homogeneous	D-mannitol		Triclinic lactose	
	Powder	Spherical	Powder	Spherical
1020±13	130±7	140±2	843±14	73±6

These results support the hypothesis that the presence of new crystal faces has a greater influence on nucleation kinetics than a change in the aspect ratio of existing crystal faces. However, there are additional factors that may contribute to the decrease or lack thereof in the induction time of AAP. One contribution to the surface morphology is the available surface area per unit mass of the substrates. Attempts were made to measure the surface area using BET, but were not successful. The purging step of the BET measurements consistently failed, preventing the analysis of the samples. Analyses using coarse approximations of the relative surface areas from the images given in Figures 5-1, 5-2, and 5-3 were inconclusive.

5.4. Epitaxy Study with EpiCalc

In a previous study on the nature of the epitaxy between two surfaces, single crystals of AAP were grown on the surface of single crystals of α-lactose monohydrate to determine which crystal faces were bound together by single crystal X-ray diffraction [35]. The bound faces were used in determining the presence or absence of lattice matching. In this study, it was not possible to determine which crystal faces were involved in the epitaxy. The spherical agglomerates were relatively small (10-50 μm) and were composed of compacted single crystals of lactose that were even smaller (<1 μm). Under these conditions it was not possible to grow a single crystal of AAP on the surface of the spherical agglomerates. In the absence of this data, the two fastest growing faces of AAP were selected, i.e. (001) and (111) [63].

EpiCalc was used to investigate potential lattice match between the lactose and AAP crystal faces. The 2D lattice parameters of the crystal faces of interest were determined. The distances and angles between concurrent lattice points for each crystal face were measured using Mercury 3.0. Epitaxy studies were performed for 16 sets of parameters for each pair of crystal faces. The 3 combinations of lattice parameters that showed a coincident lattice match are shown

in Table 5-2. The V/V_0 values are the minimum calculated potential values, and ϕ is the azimuthal angle at which the minimum V/V_0 value occurred.

Table 5-2: Lattice parameters for faces of AAP and lactose showing coincident lattice matches, and the minimum V/V0 value and the angle at which the minimum occurs

AAP face	(001)	(001)	(001)
a_1 [Å]	7.094	7.094	7.094
a_2[Å]	11.643	11.643	11.643
α [°]	52.46	52.46	52.46
Lactose Face	$(14\bar{1})$	$(14\bar{1})$	$(14\bar{1})$
b_1[Å]	7.878	7.878	27.531
b_2[Å]	29.589	38.508	29.589
β[°]	67.34	45.16	15.31
V/V_0	0.71	0.63	0.616
ϕ [°]	7.50	7.25	14.75

Though EpiCalc gives a fast method to test for a lattice match between two crystal faces, it ignores favorable molecular interactions, which can also be significant in reducing nucleation induction times. Previous studies have shown that molecular interactions can be the dominant force rather than lattice matching [35]. Molecular dynamics simulations were performed to explore the role that molecular functionality plays in enhancing nucleation kinetics by influencing epitaxy. These simulations were designed to give the same information as the EpiCalc calculations but with the inclusion of a more sophisticated energy potential energy function to account for specific molecular interactions.

5.5. Molecular Dynamics Simulations

The results of the simulations are summarized in Figures 5-7(a)–(c). The figures show the ΔE of interaction per molecule in the unit cell versus the azimuthal angle ϕ (see Figure 2-3). The ΔE was measured with reference to the total average energy of all configurations and therefore identified by how

much certain azimuthal angles were favored over others. This implies that direct comparisons between systems are only qualitative.

In Figure 5-7(a), ΔE of interaction for the (011) face of lactose is plotted with the (001) and (111) faces of AAP. These face pairings were aimed at representing the AAP-single crystal lactose system. The most abundant face of lactose (determined by XRPD intensity) was chosen and paired to the fastest growing faces of AAP. As shown in the figure, there is little variability in the interaction energy as a function of azimuthal angle. The low variability could either be a result of all azimuthal angles strongly interacting or all angles weakly interacting. To determine what the case might be we also analyzed the number of hydrogen bond pairings between the faces as a function of azimuthal angle. While this analysis cannot explain all the variability (or lack thereof) in ΔE it acts as a suggestive proxy for the systems in the present study because of the high number of potential donor/acceptor pairs. The results of this analysis are given in Figure 5-8. The number of observed hydrogen bonds for these face pairings is, on average, lower than the other face pairings simulated. This suggests that low variability in the ΔE's for the (011) face of lactose with the (001) and (111) faces of AAP is because they are interacting relatively weakly at all azimuthal angles. This is in agreement with the relatively long nucleation induction times observed for AAP in the presence of single crystal lactose.

In Figure 5-7(b) we have plotted three of the unique lactose/AAP face pairings that can occur in the presence of spherical agglomerates of lactose but not the single crystal form (as determined from the XRPD experiments). The EpiCalc calculations demonstrated the (140)/(001) and (20$\bar{1}$)(001) pairs were incommensurate. However the (14$\bar{1}$)/(001) pairing showed a coincident lattice match at an azimuthal angle of 7.25° as seen in Table 5-2. The molecular dynamics simulations also show a clear favorability for this face pairing as indicated by the large decrease in the interaction energy. The minimum in the ΔE occurs at an azimuthal angle of approximately 2.5° and not 7.25°. Though this appears to be a small discrepancy, only a few degrees can mean the difference between coincidence and incommensurism. One might suspect that such a small difference could be explained in terms of fluctuations in the structures as a

result of the molecular dynamics. However, on measuring a representative pair of vectors this was found not to be the case. On the other hand, the hydrogen bond analysis in Figure 9 suggests that the ideal azimuthal angle for hydrogen bonding occurs at –17° for this face pairing. This suggests that the stability minimum occurs at an angle of 2.5° because of an averaging effect of maximal hydrogen bonding and ideal lattice coincidence – weighted in favor of coincidence. If this is the case, it demonstrates the importance of having both molecular functionality matching and lattice matching.

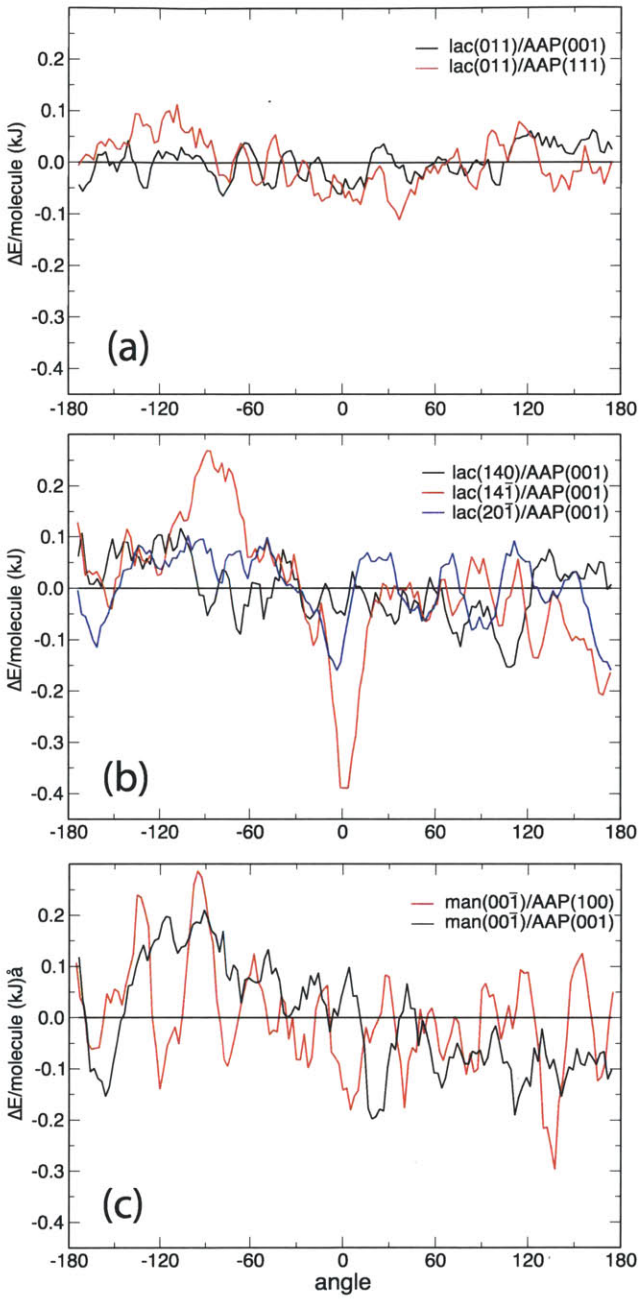

Figure 5-7: Relative Average Interaction Energy per Molecule (kJ) Between Various Crystal Faces of Lactose and AAP as a Function of the Azimuthal Angle Between Lattice vectors

The relative importance of having both molecular functionality and lattice matching to enhance stability is further demonstrated by the results of the hydrogen bond analysis of the

(20$\bar{1}$)/(001) faces in Figure 5-8. There is a very large maximum in the number of hydrogen bonds occurring at an angle of approximately –5°, resulting in a stability minimum in the interaction energy of the two faces at precisely the same angle (see Figure 5-7(b)). However, while the total number of hydrogen bonds at the maximum for the (20$\bar{1}$)/(001) faces is greater than that of the (14$\bar{1}$)/(001) faces, the lack of lattice matching between the (20$\bar{1}$) and (001) faces means the stability minimum has a smaller depth.

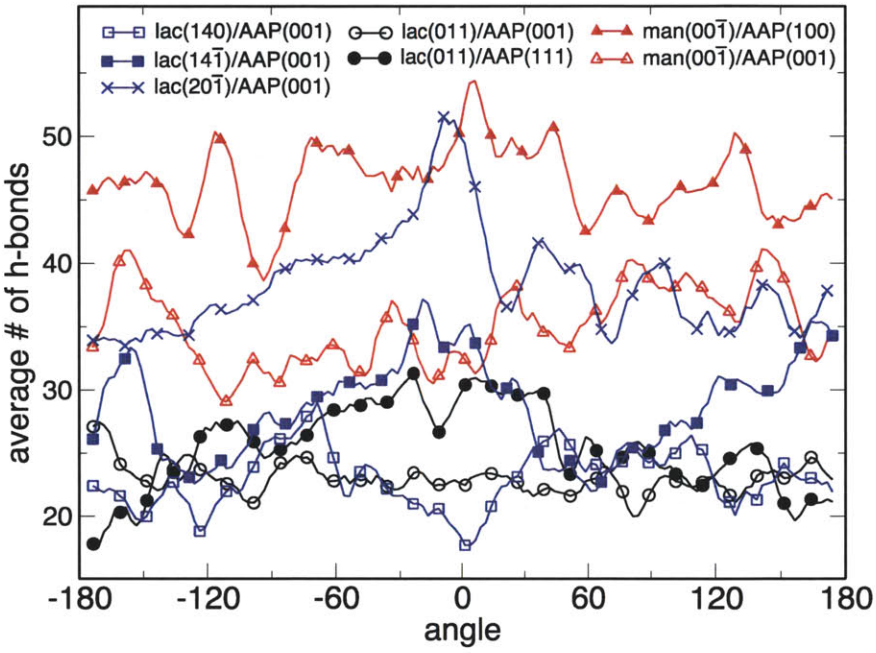

Figure 5-8: Average Number of Hydrogen Bonds Between Various Crystal Faces of Lactose and AAP as a Function of the Azimuthal Angle Between Lattice vectors.

Previous studies have shown that lattice matching is not necessary for nucleation rate enhancement by a substrate [35]. However, a lattice match in conjunction with matching molecular functionality has been shown to have a greater effect on nucleation kinetics than either of the two factors alone and is in qualitative agreement with the stability minima in Figure 5-7(b). This is further highlighted by the results in Figure 5-7(c) where we have plotted the interaction

energy of the $(00\bar{1})$ face of mannitol with the (100) face of AAP, which are known to bind together and has a similar, albeit longer, nucleation induction time. Minima in the ΔE are observed at a number of angles (-120°, -75°, 6.0°, 41.0° and 130.0°), which can be directly related to local maxima in the number of hydrogen bonds in Figure 9. The multiple minima in ΔE and their apparent strength are also in agreement with the observed low nucleation induction time for AAP in the presence of D-mannitol.

In summary, the molecular dynamics simulations show that the interaction energy from a system with both lattice matching and functionality matching – the pairing of the $(14\bar{1})/(001)$ faces – is more favorable than a system showing only functionality matching – the pairing of the $(20\bar{1})/(001)$ faces of lactose and AAP and the $(00\bar{1})/(100)$ faces of mannitol and AAP. Forming spherical agglomerates of substrates is one potential way to generate new faces and potential interactions with the crystallizing phase. This technique may provide a new way to control and enhance nucleation kinetics.

5.6. Conclusions

Generating spherical agglomerates through emulsion crystallization is a possible method to enact morphology changes of a substrate. This was demonstrated by crystallizing β-mannitol and triclinic lactose as spherical agglomerates. Crystallization of acetaminophen (AAP) in the presence of spherical agglomerates of triclinic lactose displayed enhanced nucleation kinetics when compared to the nucleation kinetics of AAP in the presence of single crystals of triclinic lactose. Crystallizations of AAP in the presence of spherical agglomerates and powder D-mannitol showed little difference in the nucleation induction time. One possible explanation for the decrease in induction time in the triclinic lactose-AAP system is the availability of new crystal faces in the spherical agglomerates. XRPD measurements of the spherical agglomerates

showed additional peaks that were attributed to the growth of additional crystal faces. Calculations were performed using EpiCalc to determine the mode of epitaxy between the new crystal faces of lactose and the fastest growing faces of AAP – the (001) and the (111) faces. Lattice matching studies indicated that the $(14\bar{1})$ face of lactose displayed partially coincident lattice matching with the (001) face of AAP. Single crystal and spherical agglomerates of D-mannitol did not show any significant difference in the available crystal faces. Furthermore, molecular dynamics simulations confirmed that the pairing of the $(14\bar{1})$/(001) faces demonstrated a far greater favourable energy interaction. These results suggest that stronger epitaxial matching can be achieved between AAP and lactose when using spherical agglomerates. Molecular computations indicated the epitaxy is driven by a combination of coincident lattice matching and the formation of extensive hydrogen bonding between the two crystal faces. This work demonstrates how the crystal morphology of a crystalline substrate is important in maximizing the effect on nucleation kinetics and that determining the 'best' crystal face for controlling epitaxy is paramount in the design of surfaces for control of heterogeneous nucleation.

6. CRYSTALLIZATION AND CHARACTERIZATION OF COMPOSITE SPHERICAL AGGLOMERATES

6.1. Introduction

Chapter 6 describes the second usage of the spherical agglomerates described in this thesis. Rather than use the spherical agglomerates as a surface for heterogeneous nucleation as in Chapter 5, this goal of this study was to make a crystal product using emulsion crystallization that would be more amenable for downstream processing, for example direct compression. Spherical particles or agglomerates have a number of physical properties that are beneficial for downstream processing. Many materials tend to crystallize in the oil phase rather than in the dispersed aqueous phase, however, so in order to increase kinetics, multiple materials were crystallized into composite spherical particles. This chapter describes the combinations of materials that were crystallized into composite spherical agglomerates, along with in-depth characterization and an analysis of a possible mechanism for the increase in kinetics.

6.2. Single Component Spherical Agglomerates

While water-in-oil emulsion crystallizations have been used in the past to create spherical agglomerates of glycine and glutamic acid hydrochloride [40], its versatility in terms of application to a wide range of compounds had not yet been demonstrated. We have addressed this issue in the current work, in which we replicated the results for glycine (Figure 2-A), and conducted additional crystallization experiments with other small hydrophilic compounds including lactose (Figure 2-B), sodium chloride (Figure 2-C), potassium chloride (Figure 2-D) and D-mannitol (2-E). All experiments used the same stirring speed (650 rpm), final crystallization temperature (80°C), and mass of additive (5 w/w%), with the target compound

concentration selected based on its solubility at 40°C, the temperature at which the aqueous solutions were prepared.

The optical microscope pictures indicate that the lactose and glycine spherical particles were highly monodisperse with virtually no crystallization in the bulk, indicating no continuous phase crystallization (Figures 6-1-A and 6-1-B). The sodium chloride and potassium chloride crystallization experiments resulted in crystallization of single crystals of the inorganic salts growing inside of the dispersed droplet without the formation of spherical agglomerates, as can be seen in Figures 6-1-C and 6-1-D. For mannitol (Figure 6-1-E), however, even though there were some spherical agglomerates, there was still a significant quantity of material that crystallized in the bulk as needles, indicated by the thin needles that crystallized outside of the droplets.

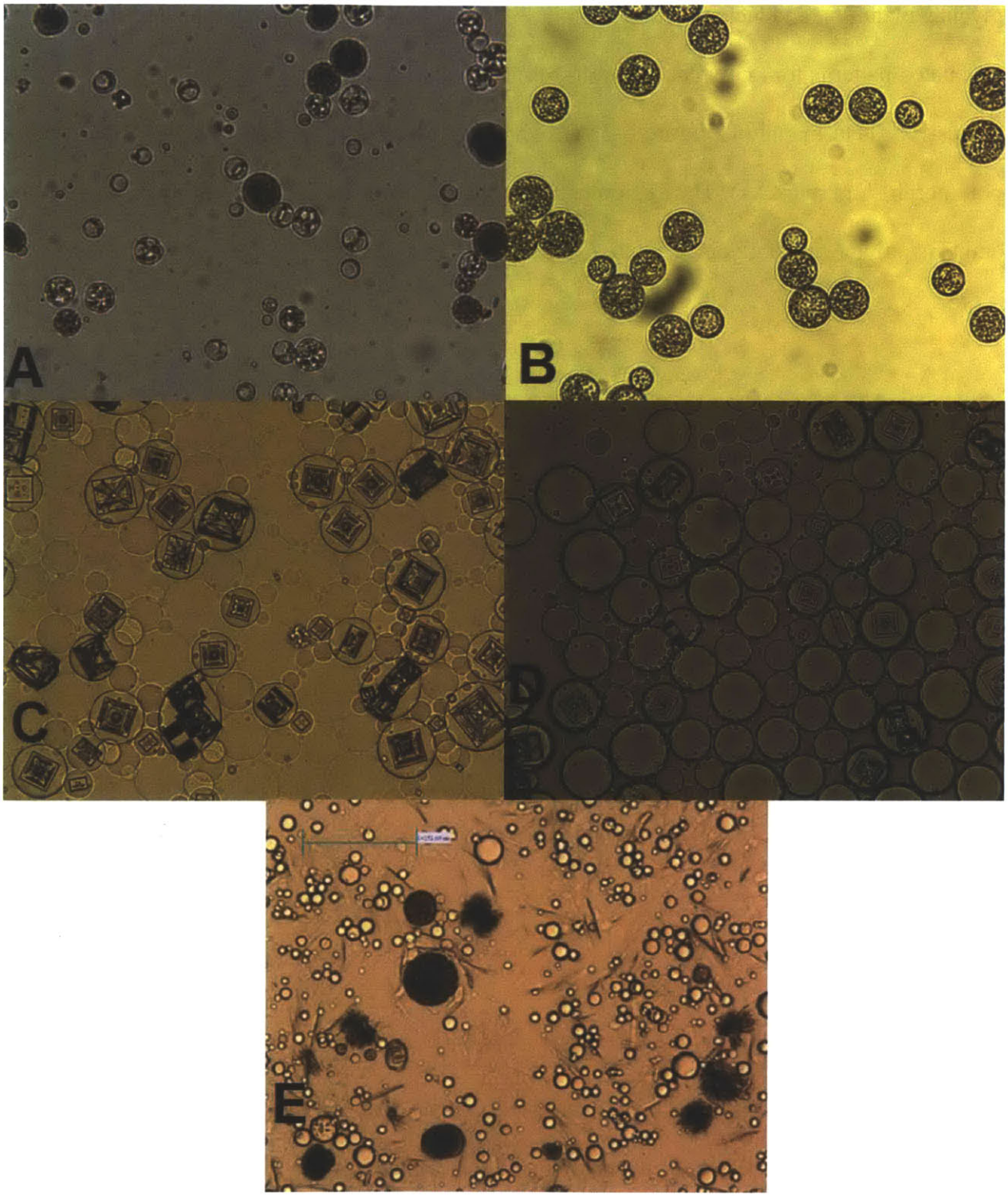

Figure 6-1: Images of attempts to make spherical agglomerates. A) Glycine B) Lactose C) Sodium Chloride D) Potassium Chloride E) Mannitol

The spherical agglomerates of glycine and lactose that were formed were further characterized using x-ray powder diffraction. Diffraction patterns for spherical agglomerates of

glycine, mannitol, and lactose can be seen in Figure 3. The diffraction patterns were compared to calculated patterns for known polymorphs of the 3 materials. The agglomerates of mannitol were exclusively beta mannitol (Figure 6-2 A), while the agglomerates of lactose were the triclinic polymorph (Figure 6-2 A). The agglomerates of glycine were found to be a mixture of the alpha and beta polymorph of glycine (Figure 6-2 B).

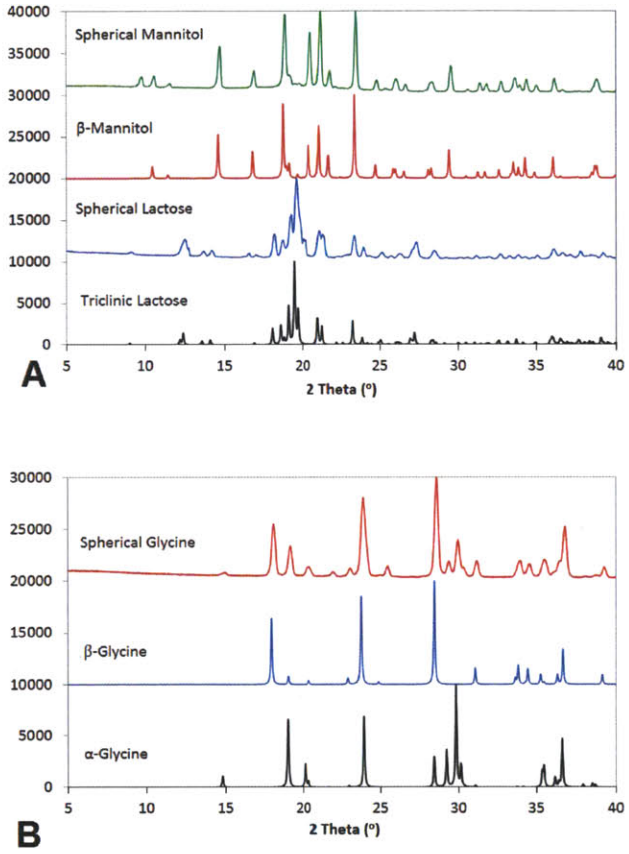

Figure 6-2: XRPD Characterization of spherical agglomerates. Calculated patterns were compared to measured patterns of spherical agglomerates for lactose and mannitol (Figure 6-1 A) and glycine (Figure 6-1 B)

Due to ease with which they crystallized as spherical agglomerates, lactose and glycine were chosen as the heterosurfaces used to induce changes in the morphologies of the other materials considered here with the goal of producing spherical agglomerates of these compounds. Mannitol was used to demonstrate that the extent of bulk crystallization could be reduced by

using heterosurfaces, while the morphologies of sodium chloride and potassium chloride crystals were completely changed from individual single crystals to spherical agglomerates.

6.3. Composite Spherical Agglomerates

Crystallization experiments were conducted using a heterosurface (lactose or glycine) to modify the morphology of the crystals formed by a target molecule (mannitol, sodium chloride, potassium chloride) in the emulsion evaporation approach. Both components were dissolved in the aqueous phase prior to creating the emulsion, with the concentration of each component adjusted to ensure that the heterosurface crystallized first. Figure 6-3 shows Optical microscope (A) and SEM images (B) of lactose/sodium chloride composite particles. It is clear that monodisperse spherical particles were generated, and that virtually no bulk nucleation of sodium chloride particles to form single crystals within the dispersed phase droplets was observed, in contrast to observations of sodium chloride crystallization in the absence of the lactose heterosurfaces. Optical microscope (Figure 6-3 C) and SEM (Figure 6-3 D) images of lactose/potassium chloride composite particles were also taken. In these images, the particles are again highly monodisperse, again with very little bulk nucleation of either material.

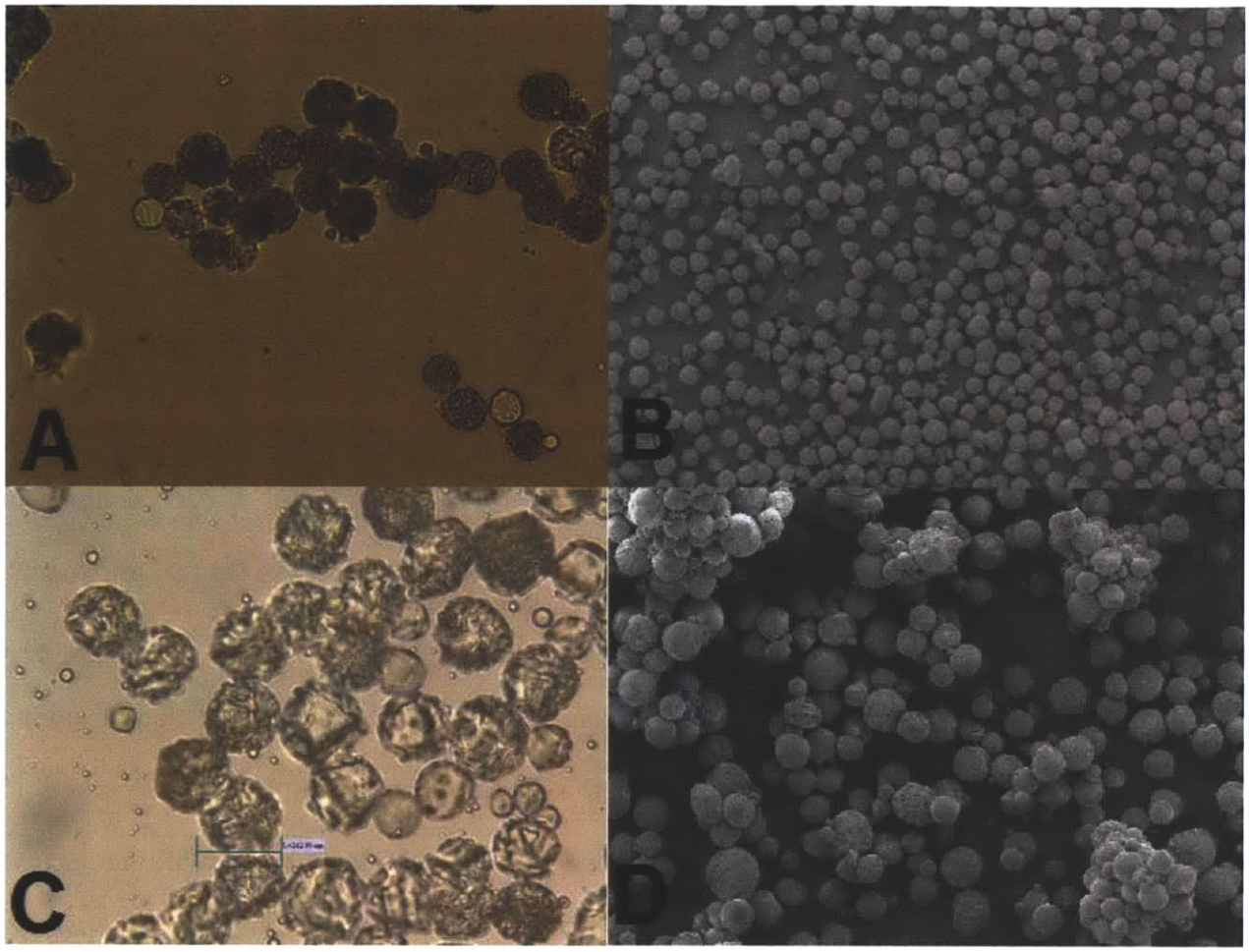

Figure 6-3: Optical microscope (A) and SEM (B) images of composite spherical agglomerates of Lactose and Sodium Chloride, optical microscope (C) and SEM (D) images of composite spherical agglomerates of Lactose and Potassium Chloride

Figure 6-4 contains optical microscope (4 A and 4 C) and SEM (4 B 4 D) images of glycine/sodium chloride and glycine/potassium chloride composite agglomerates. As seen in the optical microscope pictures, the composite particles are again quite monodisperse. Once again, the crystallization behavior has changed significantly. The sodium chloride did not crystallize as single crystals inside of the emulsion droplets. The SEM images show further proof of the spherical agglomeration of the material.

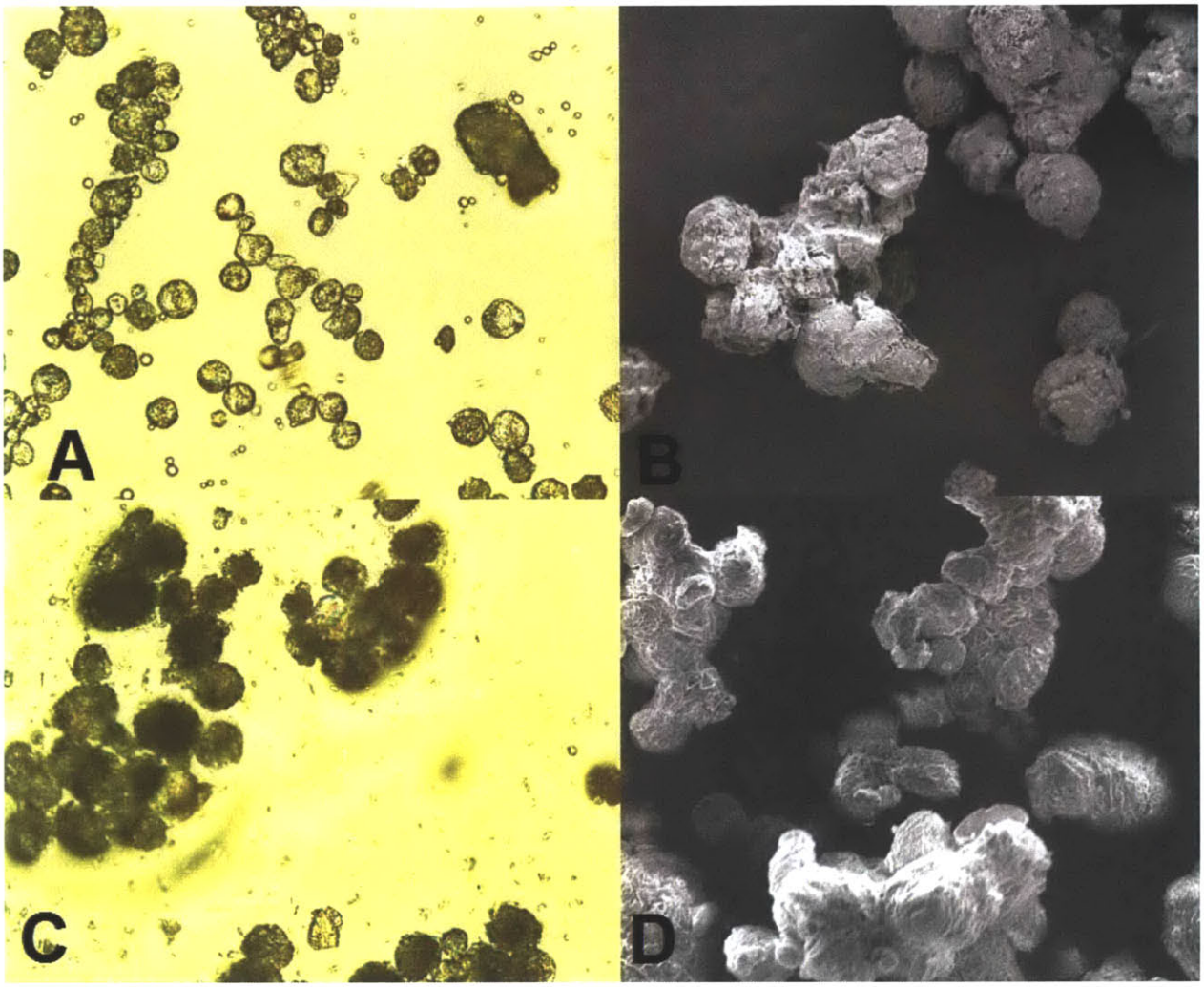

Figure 6-4: Optical microscope (A) and SEM (B) images of composite spherical agglomerates of Glycine and Sodium Chloride. Optical microscope (C) and SEM (D) images of composite spherical agglomerates of Glycine and Potassium Chloride

Glycine/Mannitol composite particles are shown in Figure 6-5, where it is evident that the majority of the crystallized material resided in the spherical agglomerates, although a small fraction of the material crystallized in the bulk. Optical microscopy (Figure 6-5 A) suggests that the bulk crystals were glycine rather than the needle-like mannitol crystals seen in Figure 6-1 E; glycine particles would be prisms. The SEM images (Figure 6-5 B), again, indicate that the majority of the material was contained in the spherical agglomerates, with no formation of bulk needle crystals.

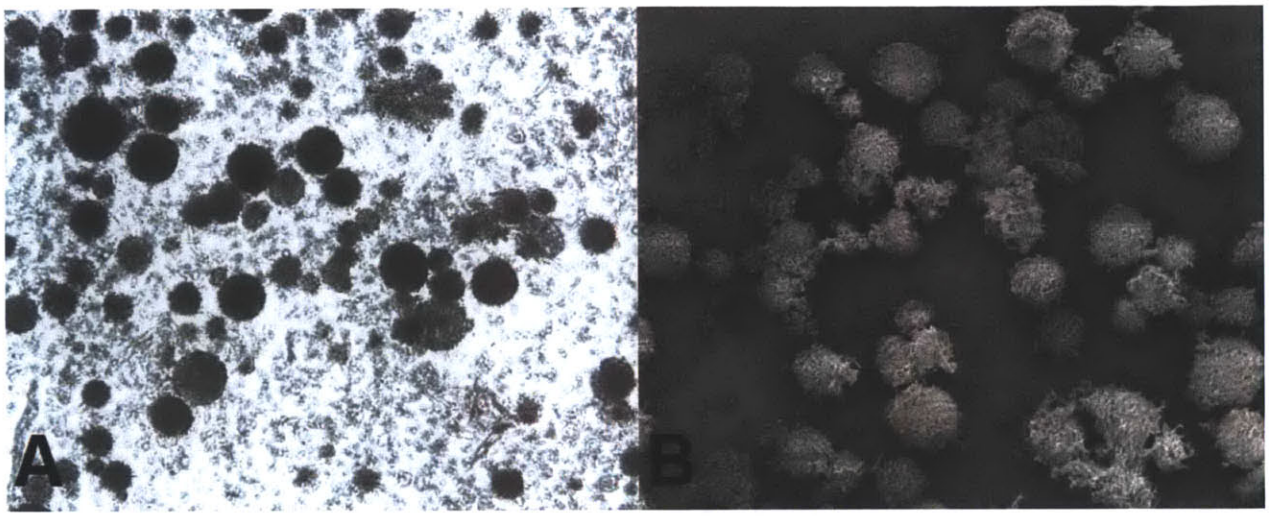

Figure 6-5: Optical microscope (A) and SEM (B) images of composite spherical agglomerates of Glycine and Mannitol

6.4. XRPD characterization of composite spherical agglomerates

X-ray powder diffraction patterns of the composite spherical particles generated in these studies were measured and compared to calculated powder patterns. The powder patterns for composite particles of lactose and glycine with potassium chloride and sodium chloride were compared with calculated powder patterns of potassium chloride and sodium chloride, as shown in Figure 6-6. The characteristic peaks of the respective inorganic salts can be identified in the diffraction pattern of each of the composite particle diffraction patterns. Combined with the crystal morphology observed in the optical microscope and SEM images, it can be inferred that the spherical particles contained both the template molecule and the target salt in the same particle. The polymorphism of lactose, which crystallized as the triclinic alpha form, did not change when it was crystallized in the presence of the inorganic salts. With glycine, however, the crystallized polymorph changed from a mixture of alpha and beta forms for the pure compound to a mixture of beta and gamma glycine when crystalized in the presence of the inorganic salts. This was not an unexpected result. Glycine crystallizations from water typically results in either the alpha or the beta form, while crystallization of glycine from solutions with increased ionic strength often results in the gamma polymorph [79, 80].

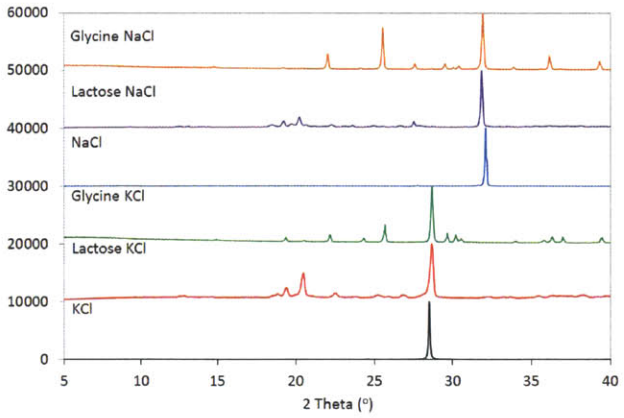

Figure 6-6: XRPD characterization of composite particles of glycine and lactose with inorganic salts. Calculated powder patterns for KCl and NaCl are included for comparison

Figure 6-7 contains the XRPD patterns for crystals obtained by emulsion crystallization with only glycine, only mannitol, and both glycine and mannitol present in the aqueous phase. From these data, it can be seen that the diffraction pattern for the glycine/mannitol spherical particles contains all of the major peaks observed in the patterns for both the spherical glycine (alpha and beta forms) and the spherical mannitol (beta polymorph) particles. This is evidence towards the crystallizations with glycine and mannitol both present resulting in agglomerates with both glycine and mannitol.

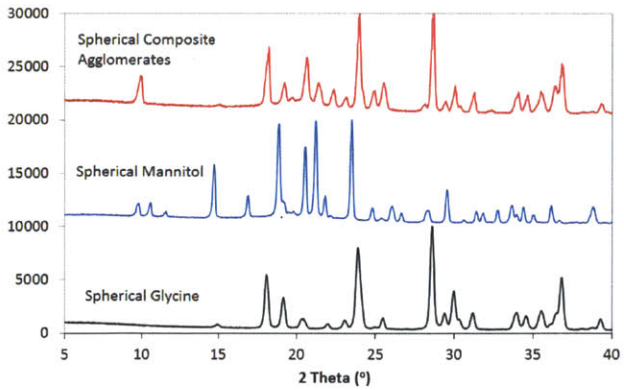

Figure 6-7: XRPD characterization of glycine/mannitol composite agglomerates. Black is spherical glycine, blue is spherical mannitol, red is composite agglomerates of glycine and mannitol

6.5. DSC Characterization of composite spherical agglomerates

Differential scanning calorimetry was used to determine whether the composite particles contained multiple components. Because of maximum temperature of the instrument, systems with the inorganic salts could not be analyzed. The melting points of both of the inorganic salts are higher than 770°C, while the maximum temperature for the DSC instrument is 400°C. Additionally, above 275°C, the glycine and mannitol began to expand and cause the lids of the DSC pans to open giving unusable data. Results for the glycine/mannitol system are shown in Figure 6-8, where the DSC melting curves for spherical glycine, spherical mannitol, and composite spherical particles are displayed. The composite particles contained two different components with significantly different melting points, both of which were close to the melting points of the spherical glycine and mannitol, respectively. The small shift the melting points of the components of a eutectic mixture will be shifted from that of the pure components.

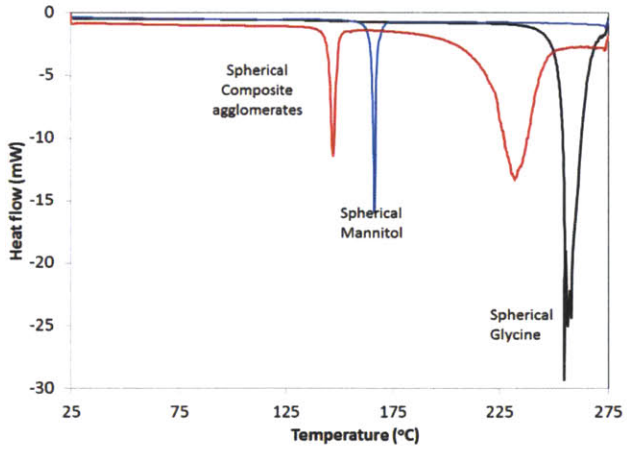

Figure 6-8: DSC characterization of glycine/mannitol composite agglomerates. Melting curves for spherical glycine, spherical mannitol, and spherical composite agglomerates are shown

6.6. Closing

This emulsion crystallization technique has been shown to be capable of generating spherical agglomerates of aqueous soluble materials. This study has shown that by using heterosurfaces as templates, composite spherical agglomerates can be made using materials that otherwise crystallize as single crystals in the emulsion droplets. This crystallization technique could potentially be expanded to the crystallization of composite particles containing larger organic molecules, including API's to enhance their mechanical properties. There is a need to characterize the physical properties of the composite particles i.e. compressibility, dissolution, or flowability, more fully in order to assess whether further process development would be beneficial. Finally, new technologies must be developed to scale up these approaches for use in actual manufacturing process.

6.7. Conclusions

Crystal morphology is a significant factor in the ease of processing of active pharmaceutical ingredients, with spherical particles or agglomerates having particularly favorable properties. This work has explored using heterosurfaces to modify the morphology of a crystallizing phase to form spherical agglomerates. Single component experiments showed that lactose and glycine could be crystallized successfully as spherical agglomerates, while potassium and sodium chloride crystallized as single crystals in the emulsion droplets. D-mannitol crystallized as spherical agglomerates, though with larger amounts of bulk crystallization than lactose or glycine. Lactose and glycine crystals were used as heterosurfaces, for the nucleation of D-mannitol, potassium chloride, and sodium chloride crystals with morphology modification. The combinations of lactose and glycine with the inorganic salts resulted in monodisperse composite agglomerates, as confirmed through x-ray powder diffraction and image analysis.

Crystallizing glycine and mannitol together also resulted in composite spherical agglomerates, as confirmed through x-ray powder diffraction, image analysis, and differential scanning calorimetry.

7. CONCLUSIONS AND FUTURE WORK

7.1. Conclusions

This thesis encompassed two major areas of research. The first area was about process development of continuous crystallizations using existing technology as part of an effort to develop continuous manufacturing for pharmaceuticals. The second area was to research new technologies and methods that could simplify and improve crystallization processes. Though they are greatly different projects, both of these areas are of vast importance to developing and implementing continuous manufacturing throughout the pharmaceutical industry.

Two different continuous crystallization processes were developed for the continuous manufacturing unit. The first process was an anti-solvent crystallization for intermediate purification. The second process was a reactive and cooling crystallization for the generation and isolation of the final product. There were significant technical challenges to overcome for both of these process development steps, but both were successfully developed and implemented into the bench-scale continuous manufacturing unit. Population and mass balances were used to model both of the crystallizations and extract important kinetic parameters. Distribution coefficients were also measured and included in the modeling. The distribution coefficients and kinetics parameters were used to simulate how changing various operating parameters would affect the crystallization yield and purity.

Two separate projects using spherical agglomerates were also researched. The first project studied the effects of morphology changes (due to crystallizing substrates as spherical agglomerates rather than as single crystals) on nucleation kinetics. Spherical agglomerates of lactose were found to have significantly different surface morphology as well as the growth of new crystal faces. Additionally, crystallizations of AAP in the presence of spherical

agglomerates of lactose were found to have faster nucleation kinetics than crystallizations of AAP in the presence of single crystal lactose. An epitaxy study between the new crystal faces of lactose and the fastest growing faces of AAP was performed. Molecular dynamics simulations were performed to measure the energy interactions between the various faces. The most stable pairing of faces ($(14\bar{1})/(001)$) was also the pair that showed the most favorable lattice match from the epitaxy study. Generating nucleation substrates as spherical agglomerates is a potential way for pre-processing of materials to improve crystallization processes.

The second study looked at making composite spherical agglomerates for downstream manufacturing purposes. Many materials cannot be crystallized as spherical agglomerates using conventional techniques. This study aimed to use heterosurfaces to template the nucleation of model compounds into spherical agglomerates. Glycine and lactose were used as heterosurfaces to template the nucleation of sodium chloride, potassium chloride, and mannitol and modify their morphology into spherical agglomerates. These agglomerates were characterized using image analysis, x-ray powder diffraction, and differential scanning calorimetry.

7.2. Future outlook

The results of this study have shown both that existing technologies are viable for continuous crystallization process development and that new techniques and methods can be developed to improve said crystallization processes. Though the process development work itself was a success, there is still some room for improvement and further research. In order to improve process yields, adding in recycle streams would be greatly beneficial. Though it comes at a potential cost with regards to purity (as soon from the modeling results), if carefully done, adding in combined evaporation and recycle step into the second vessel could result in significantly higher yields for both of the crystallizations. The crystallization for the Aliskiren

boc-base would be more difficult to design, as the solvent is a mixed solvent and thus the evaporation would have to be more finely controlled. Additionally, developing online process analytical technology to perform real time monitoring of the crystallizations would be beneficial. Attempts were made to use both mid-IR and NIR spectroscopic probes inside of the crystallizers as well as online FBRM measurements. The main issue with those was that the probe window was clogged by the slurry, preventing any measurements. There were a few potential research tools that could automatically clean the probe window, but further investigation into new methods would be of great help. Finally, the modeling was performed using a 1-dimensional size model. The crystals from both of the crystallizations were in fact needles, which cannot truly be defined by a 1 dimension. The development of a more complex 2-dimensional model for the crystallization would be beneficial in order to more accurately describe the behavior of the crystallization.

8. REFERENCES

1. DiMasi, J.A., R.W. Hansen, and H.G. Grabowski, *The price of innovation: new estimates of drug development costs.* Journal of Health Economics, 2003. **22**(2): p. 151-185.
2. McIntyre, A.-M., *Key issues in the pharmaceutical industry*. 1999, Chichester ; New York: John Wiley & Sons, Ltd. vii, 216 p.
3. Behr, A., et al., *New developments in chemical engineering for the production of drug substances.* Engineering in Life Sciences, 2004. **4**(1): p. 15-24.
4. Kockmann, N., et al., *Enabling continuous-flow chemistry in microstructured devices for pharmaceutical and fine-chemical production.* Chemistry-a European Journal, 2008. **14**(25): p. 7470-7477.
5. Roberge, D.M., et al., *Microreactor technology and continuous processes in the fine chemical and pharmaceutical industry: Is the revolution underway?* Organic Process Research & Development, 2008. **12**(5): p. 905-910.
6. Kockmann, N. and D.M. Roberge, *Harsh Reaction Conditions in Continuous-Flow Microreactors for Pharmaceutical Production.* Chemical Engineering & Technology, 2009. **32**(11): p. 1682-1694.
7. Alvarez, A.J. and A.S. Myerson, *Continuous Plug Flow Crystallization of Pharmaceutical Compounds.* Crystal Growth & Design, 2010. **10**(5): p. 2219-2228.
8. Alvarez, A.J., A. Singh, and A.S. Myerson, *Crystallization of Cyclosporine in a Multistage Continuous MSMPR Crystallizer.* Crystal Growth & Design, 2011. **11**(10): p. 4392-4400.
9. Brettmann, B., et al., *Solid-state NMR characterization of high-loading solid solutions of API and excipients formed by electrospinning.* J Pharm Sci, 2012. **101**(4): p. 1538-45.
10. Buschle-Diller, G., et al., *Release of antibiotics from electrospun bicomponent fibers.* Cellulose, 2007. **14**(6): p. 553-562.
11. Leuenberger, H., *New trends in the production of pharmaceutical granules: batch versus continuous processing.* European Journal of Pharmaceutics and Biopharmaceutics, 2001. **52**(3): p. 289-296.
12. Vervaet, C. and J.P. Remon, *Continuous granulation in the pharmaceutical industry.* Chemical Engineering Science, 2005. **60**(14): p. 3949-3957.
13. Myerson, A.S., *Handbook of industrial crystallization*. 2002, Butterworth-Heinemann: Boston.
14. Jones, A.G., *Crystallization process systems*. 2002, Oxford: Butterworth-Heinemann.

15. Mullin, J.W., *Crystallization.* 2001, Butterworth-Heinemann: Oxford ; Boston.
16. Nyvlt, J., *Solid-Liquid Phase Equilibria.* 1977: Elsevier Science Ltd.
17. Nývlt, J., *Design of Crystallizers.* 1992, University of Michigan: CRC Press.
18. Randolph, A.D. and M.A. Larson, *Theory of particulate processes : analysis and techniques of continuous crystallization.* 2nd ed. 1988, San Diego: Academic Press. xv, 369 p.
19. Chen, J., et al., *Pharmaceutical Crystallization.* Crystal Growth & Design, 2011. **11**(4): p. 887-895.
20. Tavare, N.S., *Crystallization Kinetics from Transients of an Msmpr Crystallizer.* Canadian Journal of Chemical Engineering, 1986. **64**(5): p. 752-758.
21. Sheikh, A.Y. and A.G. Jones, *Optimal synthesis of stagewise continuous crystallization process networks.* Aiche Journal, 1998. **44**(7): p. 1637-1645.
22. Lawton, S., et al., *Continuous Crystallization of Pharmaceuticals Using a Continuous Oscillatory Baffled Crystallizer.* Organic Process Research & Development, 2009. **13**(6): p. 1357-1363.
23. Hanley, T.R. and R.A. Mischke, *Mixing Model for a Continuous-Flow Stirred Tank Reactor.* Industrial & Engineering Chemistry Fundamentals, 1978. **17**(1): p. 51-58.
24. Zhang, H.T., et al., *Development of Continuous Anti-Solvent/Cooling Crystallization Process using Cascaded Mixed Suspension, Mixed Product Removal Crystallizers.* Organic Process Research & Development, 2012. **16**(5): p. 915-924.
25. Quon, J.L., et al., *Continuous Crystallization of Aliskiren Hemifumarate.* Crystal Growth & Design, 2012. **12**(6): p. 3036-3044.
26. Ward, M.D. and L. Yu, *Selective nucleation and discovery of organic polymorphs through epitaxy.* Abstracts of Papers of the American Chemical Society, 2002. **223**: p. U645-U645.
27. Chadwick, K., A. Myerson, and B. Trout, *Polymorphic control by heterogeneous nucleation - A new method for selecting crystalline substrates.* Crystengcomm, 2011. **13**(22): p. 6625-6627.
28. Aizenberg, J., A.J. Black, and G.M. Whitesides, *Control of crystal nucleation by patterned self-assembled monolayers.* Nature, 1999. **398**(6727): p. 495-498.
29. Carter, P.W. and M.D. Ward, *Directing Polymorph Selectivity during Nucleation of Anthranilic Acid on Molecular Substrates.* Journal of the American Chemical Society, 1994. **116**(2): p. 769-770.

30. Mitchell, C.A., L. Yu, and M.D. Ward, *Selective nucleation and discovery of organic polymorphs through epitaxy with single crystal substrates.* Journal of the American Chemical Society, 2001. **123**(44): p. 10830-10839.
31. Price, C.P., A.L. Grzesiak, and A.J. Matzger, *Crystalline polymorph selection and discovery with polymer heteronuclei.* Journal of the American Chemical Society, 2005. **127**(15): p. 5512-5517.
32. Diao, Y., et al., *Controlled Nucleation from Solution Using Polymer Microgels.* Journal of the American Chemical Society, 2011. **133**(11): p. 3756-3759.
33. Diao, Y., et al., *Surface Design for Controlled Crystallization: The Role of Surface Chemistry and Nanoscale Pores in Heterogeneous Nucleation.* Langmuir, 2011. **27**(9): p. 5324-5334.
34. Diao, Y., et al., *Nucleation under Soft Confinement: Role of Polymer-Solute Interactions.* Crystal Growth & Design, 2012. **12**(1): p. 508-517.
35. Chadwick, K., et al., *Toward the Rational Design of Crystalline Surfaces for Heteroepitaxy: Role of Molecular Functionality.* Crystal Growth & Design, 2012. **12**(3): p. 1159-1166.
36. Zhang, H.T., et al., *Investigation on the Spherical Crystallization Process of Cefotaxime Sodium.* Industrial & Engineering Chemistry Research, 2010. **49**(3): p. 1402-1411.
37. Amaro-Gonzalez, D. and B. Biscans, *Spherical agglomeration during crystallization of an active pharmaceutical ingredient.* Powder Technology, 2002. **128**(2-3): p. 188-194.
38. Di Martino, P., et al., *Improved dissolution behavior of fenbufen by spherical crystallization.* Drug Development and Industrial Pharmacy, 1999. **25**(10): p. 1073-1081.
39. Kawashima, Y., *Spherical Crystallization and Pharmaceutical Systems.* Pharmacy International, 1984. **5**(2): p. 40-43.
40. Chadwick, K., R.J. Davey, and R. Mughal, *Crystallisation from Water-in-Oil Emulsions As a Route to Spherical Particulates: Glycine and the Hydrochloride Salts of Glutamic Acid and Ephedrine.* Organic Process Research & Development, 2009. **13**(6): p. 1284-1290.
41. Ward, M.D., *Bulk crystals to surfaces: Combining X-ray diffraction and atomic force microscopy to probe the structure and formation of crystal interfaces.* Chemical Reviews, 2001. **101**(6): p. 1697-1725.
42. Hooks, D.E., T. Fritz, and M.D. Ward, *Epitaxy and molecular organization on solid substrates.* Advanced Materials, 2001. **13**(4): p. 227-+.
43. Kawashima, Y., et al., *Crystal modification of phenytoin with polyethylene glycol for improving mechanical strength, dissolution rate and*

bioavailability by a spherical crystallization technique. Chem Pharm Bull (Tokyo), 1986. **34**(8): p. 3376-83.
44. Kawashima, Y., et al., *Improved flowability and compactibility of spherically agglomerated crystals of ascorbic acid for direct tableting designed by spherical crystallization process.* Powder Technology, 2003. **130**(1-3): p. 283-289.
45. Kawashima, Y., M. Okumura, and H. Takenaka, *Spherical Crystallization - Direct Spherical Agglomeration of Salicylic-Acid Crystals during Crystallization.* Science, 1982. **216**(4550): p. 1127-1128.
46. Kawashima, Y., et al., *Spherical Crystallization .4. An Experimental-Study of the Kinetics of the Spherical Crystallization of Sodium Theophylline Monohydrate.* Powder Technology, 1983. **34**(2): p. 255-260.
47. Kawashima, Y., et al., *Direct preparation of spherically agglomerated salicylic acid crystals during crystallization.* J Pharm Sci, 1984. **73**(11): p. 1535-8.
48. Kawashima, Y., et al., *Preparations of agglomerated crystals of polymorphic mixtures and a new complex of indomethacin-epirizole by the spherical crystallization technique.* J Pharm Sci, 1985. **74**(11): p. 1152-6.
49. Toldy, A.I., et al., *Spherical Crystallization of Glycine from Monodisperse Microfluidic Emulsions.* Crystal Growth & Design, 2012.
50. Carter, P.W. and M.D. Ward, *Topographically Directed Nucleation of Organic-Crystals on Molecular Single-Crystal Substrates.* Journal of the American Chemical Society, 1993. **115**(24): p. 11521-11535.
51. Diao, Y., et al., *Towards surface design to control crystallization: Understanding the roles of surface chemistry and morphology in heterogeneous nucleation.* Abstracts of Papers of the American Chemical Society, 2010. **240**.
52. Trifkovic, M., M. Sheikhzadeh, and S. Rohani, *Kinetics estimation and single and multi-objective optimization of a seeded, anti-solvent, isothermal batch crystallizer.* Industrial & Engineering Chemistry Research, 2008. **47**(5): p. 1586-1595.
53. Ruf, A., J. Worlitschek, and M. Mazzotti, *Modeling and experimental analysis of PSD measurements through FBRM.* Particle & Particle Systems Characterization, 2000. **17**(4): p. 167-179.
54. Nie, Q., J.K. Wang, and Q.X. Yin, *Effect of solution thermodynamics on the purification of two isomorphic steroids by solution crystallization.* Chemical Engineering Science, 2006. **61**(18): p. 5962-5968.
55. Sheikh, A.Y. and A.G. Jones, *Crystallization process optimization via a revised machine learning methodology.* Aiche Journal, 1997. **43**(6): p. 1448-1457.

56. Garside, J. and S.J. Jancic, *Prediction and Measurement of Crystal Size Distribution for Size-Dependent Growth.* Chemical Engineering Science, 1978. **33**(12): p. 1623-1630.
57. Togkalidou, T., et al., *Parameter estimation and optimization of a loosely bound aggregating pharmaceutical crystallization using in situ infrared and laser backscattering measurements.* Industrial & Engineering Chemistry Research, 2004. **43**(19): p. 6168-6181.
58. Leyssens, T., C. Baudry, and M.L.E. Hernandez, *Optimization of a Crystallization by Online FBRM Analysis of Needle-Shaped Crystals.* Organic Process Research & Development, 2011. **15**(2): p. 413-426.
59. Yi, Y.J., et al., *Development of a small-scale automated solubility measurement apparatus.* Industrial & Engineering Chemistry Research, 2005. **44**(15): p. 5427-5433.
60. Hillier, A.C. and M.D. Ward, *Epitaxial interactions between molecular overlayers and ordered substrates.* Physical Review B, 1996. **54**(19): p. 14037-14051.
61. Last, J.A., et al., *The physicochemical origins of coincident epitaxy in molecular overlayers: Lattice modeling vs potential energy calculations.* Journal of Physical Chemistry B, 1999. **103**(32): p. 6723-6733.
62. http://www.nyu.edu/fas/dept/chemistry/wardgroup/Software.html#EpiCalc.
63. Nichols, G. and C.S. Frampton, *Physicochemical characterization of the orthorhombic polymorph of paracetamol crystallized from solution.* Journal of Pharmaceutical Sciences, 1998. **87**(6): p. 684-693.
64. Kirschner, K.N., et al., *GLYCAM06: a generalizable biomolecular force field. Carbohydrates.* J Comput Chem, 2008. **29**(4): p. 622-55.
65. Bayly, C.I., et al., *A Well-Behaved Electrostatic Potential Based Method Using Charge Restraints for Deriving Atomic Charges - the Resp Model.* Journal of Physical Chemistry, 1993. **97**(40): p. 10269-10280.
66. Wang, J.M., et al., *Automatic atom type and bond type perception in molecular mechanical calculations.* Journal of Molecular Graphics & Modelling, 2006. **25**(2): p. 247-260.
67. Cornell, W.D., et al., *A second generation force field for the simulation of proteins, nucleic acids, and organic molecules (vol 117, pg 5179, 1995).* Journal of the American Chemical Society, 1996. **118**(9): p. 2309-2309.
68. Wang, J.M., et al., *Development and testing of a general amber force field.* Journal of Computational Chemistry, 2004. **25**(9): p. 1157-1174.
69. Hess, B., et al., *GROMACS 4: Algorithms for highly efficient, load-balanced, and scalable molecular simulation.* Journal of Chemical Theory and Computation, 2008. **4**(3): p. 435-447.

70. Sorin, E.J. and V.S. Pande, *Exploring the helix-coil transition via all-atom equilibrium ensemble simulations.* Biophysical Journal, 2005. **88**(4): p. 2472-2493.
71. Frisch, M.J., et al., *Gaussian 03*. 2004: Wallingford, CT. p. Gaussian, Inc
72. Essmann, U., et al., *A Smooth Particle Mesh Ewald Method.* Journal of Chemical Physics, 1995. **103**(19): p. 8577-8593.
73. Hess, B., et al., *LINCS: A linear constraint solver for molecular simulations.* Journal of Computational Chemistry, 1997. **18**(12): p. 1463-1472.
74. Nere, N.K., et al., *Transformation of the chord-length distributions to size distributions for nonspherical particles with orientation bias.* Industrial & Engineering Chemistry Research, 2007. **46**(10): p. 3041-3047.
75. Dang, L.P., et al., *Solubility of Fumaric Acid in Propan-2-ol, Ethanol, Acetone, Propan-1-ol, and Water.* Journal of Chemical and Engineering Data, 2009. **54**(11): p. 3112-3113.
76. Barlow, T.W. and A.D.J. Haymet, *Alta - an Automated Lag-Time Apparatus for Studying the Nucleation of Supercooled Liquids.* Review of Scientific Instruments, 1995. **66**(4): p. 2996-3007.
77. Laval, P., A. Crombez, and J.B. Salmon, *Microfluidic Droplet Method for Nucleation Kinetics Measurements.* Langmuir, 2009. **25**(3): p. 1836-1841.
78. Knezic, D., J. Zaccaro, and A.S. Myerson, *Nucleation induction time in levitated droplets.* Journal of Physical Chemistry B, 2004. **108**(30): p. 10672-10677.
79. Lian, Y. and N.G. Kingman, *Glycine crystallization during spray drying: The pH effect on salt and polymorphic forms.* Journal of Pharmaceutical Sciences, 2002. **91**(11): p. 2367-2375.
80. Akers, M.J., et al., *Glycine Crystallization during Freezing - the Effects of Salt Form, Ph, and Ionic-Strength.* Pharmaceutical Research, 1995. **12**(10): p. 1457-1461.